Magnetic topological insulators

Yoshinori Tokura[1,2]*, *Kenji Yasuda*[2] *and Atsushi Tsukazaki*[3]

Abstract | The importance of global band topology is unequivocally recognized in condensed matter physics, and new states of matter, such as topological insulators, have been discovered. Owing to their bulk band topology, 3D topological insulators possess a massless Dirac dispersion with spin–momentum locking at the surface. Although 3D topological insulators were originally proposed in time-reversal invariant systems, the onset of a spontaneous magnetization or, equivalently, a broken time-reversal symmetry leads to the formation of an exchange gap in the Dirac band dispersion. In such magnetic topological insulators, tuning of the Fermi level in the exchange gap results in the emergence of a quantum Hall effect at zero magnetic field, that is, of a quantum anomalous Hall effect. Here, we review the basic concepts of magnetic topological insulators and their experimental realization, together with the discovery and verification of their emergent properties. In particular, we discuss how the development of tailored materials through heterostructure engineering has made it possible to access the quantum anomalous Hall effect, the topological magnetoelectric effect, the physics related to the chiral edge states that appear in these materials and various spintronic phenomena. Further theoretical and experimental research on magnetic topological insulators will provide fertile ground for the development of new concepts for next-generation electronic devices for applications such as spintronics with low energy consumption, dissipationless topological electronics and topological quantum computation.

The dynamics of conduction electrons in magnetic solids, in particular the quantum transport of spin, has attracted much attention in the past few decades, for example, in the context of heavy-fermion systems[1], high-temperature superconductors[2], giant magnetoresistance systems[3], colossal magnetoresistance oxides[4] and diluted magnetic semiconductors[5]. Some of these systems, in particular those exhibiting giant and colossal magnetoresistance, have already found industrial applications. More recently, another branch of work on quantum transport based on the concept of topology has emerged. These two lines of research are now merging, producing new fields and directions; one example is the study of magnetic topological insulators (TIs).

There is an increasing interest in topological quantum materials, which exhibit electronic or magnetic states characterized by an integer topological invariant, such as the Chern number and the Z_2 invariant for the topological electronic structure in momentum space[6,7] and the skyrmion number, defined by the winding number of the spin configuration, in real space[8]. One distinguishing feature of topological materials is the presence of electronic or magnetic states that are robust against external perturbations thanks to the topological protection afforded by the fact that the integer topological number is invariant under continuous deformations.

The first example of a topological state observed in condensed matter was the integer quantum Hall effect (QHE) — an analogue of the ordinary Hall effect in which the Hall conductance is quantized — measured in 2D electron systems in a magnetic field[9]. The experimental results were interpreted on the basis of the concept of topology introduced in the Thouless–Kohmoto–Nightingale–den Nijs (TKNN)[10,11] theory. The TKNN formula for a 2D electron system with broken time-reversal symmetry is characterized by the topological invariant called the TKNN number or Chern number (C), which, in the integer QHE, corresponds to the occupancy of the Landau levels. The Hall conductivity σ_{xy} is expressed as $\sigma_{xy} = \frac{Ce^2}{h}$, where e is the electron charge and h is Planck's constant. Because C is an integer, there is no deformation of the material parameters that can continuously connect it to a trivial insulator with $C = 0$ or to a vacuum (that also has $C = 0$). Owing to a phenomenon known as bulk–boundary correspondence, this results in the appearance of a gapless state at the sample edge that forms a number $|C|$ of chiral edge channels. Charge transport in these edge channels is non-dissipative, and its direction (clockwise or anticlockwise) is uniquely determined by the sign of the charge (electron or hole) and by the direction of an applied magnetic field (up or down).

[1]*RIKEN Center for Emergent Matter Science (CEMS), Wako, Japan.*

[2]*Department of Applied Physics, University of Tokyo, Tokyo, Japan.*

[3]*Institute for Materials Research, Tohoku University, Sendai, Japan.*

**e-mail: tokura@riken.jp*

https://doi.org/10.1038/s42254-018-0011-5

Key points

- The chemical doping of topological insulators with transition metal elements induces a spontaneous magnetization that interacts with the topological surface state to open a mass gap at the Dirac point.
- The precise tuning of the Fermi level at the mass gap enables the observation of the quantum anomalous Hall effect — a zero-magnetic-field quantum Hall effect arising in the presence of a spontaneous magnetization — which is further stabilized by heterostructure engineering.
- Chiral edge conduction associated with the quantum anomalous Hall effect is manipulated by magnetic domain walls, and the edge modes can be turned into chiral Majorana edge modes via proximity coupling with a superconductor.
- Heterostructure engineering and terahertz measurements enable the observation of the quantized topological magnetoelectric effect.
- The spin–momentum-locked conduction electrons in the surface state lead to versatile spintronic functionalities, such as an efficient generation of spin transfer torque, as a result of charge-to-spin conversion.
- The further development of materials design and engineering will realize the quantum anomalous Hall effect at higher temperatures, the control of this state with external fields and exotic topological states of matter.

From the analogy between the ordinary Hall effect and anomalous Hall effect (AHE), which are induced by an external magnetic field and a spontaneous magnetization, respectively, it was natural to ask whether a quantum AHE (QAHE) — an integer QHE at zero magnetic field — could be achieved. Initially, the QAHE was theoretically predicted to arise in honeycomb and kagome lattices with staggered magnetic fluxes[12,13]. These fluxes lead to the formation of a gapped state, the quantum Hall insulator, giving a Berry curvature of the conduction electrons.

Meanwhile, regarding the intrinsic mechanism underlying the AHE, an interpretation in terms of the TKNN formula for an electronic band with relativistic spin–orbit coupling was established in 2D as well as 3D systems[14,29]: σ_{xy} for the intrinsic AHE is given by the integration of the Berry curvature $b_n(\boldsymbol{k}) = \nabla \times a_n(\boldsymbol{k})$, where $a_n(\boldsymbol{k}) = i\left\langle u_{n\boldsymbol{k}}\middle|\frac{\partial}{\partial \boldsymbol{k}}\middle|u_{n\boldsymbol{k}}\right\rangle$ is the Berry connection (u_{nk} is the periodic part of the Bloch function of the nth band) over the occupied states in the Brillouin zone, just as in the TKNN formula. Considering the close similarity between the QHE and AHE, it was predicted that the QAHE would be readily materialized in a 2D ferromagnet with spin–orbit coupling if gapping or full carrier localization at the Fermi level (E_F) was realized[15]. However, the experimental discovery of the QAHE[16] had to await the successful growth of a ferromagnetic TI following the theoretical design and prediction[6,7,17,18].

TIs were theoretically discovered by extending the formalism for 2D (TKNN) topological phases with broken time-reversal symmetry to 2D or 3D systems with time-reversal symmetry[19–22]. The topological number in this case is the Z_2 index, which has values $\nu_2 = 0$ or 1, unlike the TKNN number, ν, which can take any integer value. $\nu_2 = 1$ corresponds to a TI, whereas $\nu_2 = 0$ corresponds to a trivial insulator or vacuum. A necessary condition for the appearance of topologically protected edge states is the presence of a band inversion between the conduction and valence band by a spin–orbit interaction that leads to the opening of a bandgap, rather than to a semimetal state with overlapping bands. Reflecting the discontinuity of ν_2 at the surface of the topological material, a gapless 2D state appears at the surface of a 3D TI or at its interface with a trivial insulator (FIG. 1a,b). Therefore, if E_F lies within the bulk bandgap, the TI shows metallic conduction at the surface (or interface) but is insulating in the bulk. The 2D surface state is described by the Hamiltonian

$$H = v_F\left(-k_y\sigma_x + k_x\sigma_y\right) \tag{1}$$

where vF is the Fermi velocity of the linear dispersion and σx and σy are the Pauli matrices for spin. This Hamiltonian implies the spin–momentum locking of the massless Dirac electrons (FIG. 1a), which means that electrons of opposite spins travel in opposite directions. Currently, many 3D TIs are known[23,24], including Bi_xSb_{1-x}, tetradymites such as Bi_2Se_3, Bi_2Te_3 and Sb_2Te_3, and strained HgTe. For these materials, a massless Dirac dispersion with spin–momentum locking has been theoretically predicted[21,25] and then experimentally confirmed with surface-sensitive probes, such as angle-resolved (and spin-resolved) photoemission spectroscopy and scanning tunnelling spectroscopy[6,7].

Introducing a spontaneous magnetization into (or next to) the surface of a TI brings about important modifications to the electronic structure of the surface, because the conduction electrons couple with the magnetization via an exchange interaction, as described by the model Hamiltonian[6,17]

$$H = v_F\left(-k_y\sigma_x + k_x\sigma_y\right) + m\sigma_z = \boldsymbol{R}\cdot\boldsymbol{\sigma} \tag{2}$$

with $\boldsymbol{R} = \left(-v_F k_y,\ v_F k_x,\ m\right)$. The exchange interaction breaks time-reversal symmetry, causing the opening of a mass gap m in the Dirac surface state (FIG. 1c), which causes the Dirac fermions in the surface state to become massive. In this 2D system with broken time-reversal symmetry, the Chern number can be defined[10] using $\hat{\boldsymbol{R}} = \boldsymbol{R}/|\boldsymbol{R}|$ as

$$C = 2\int_{BZ}\hat{\boldsymbol{R}}\cdot\left(\frac{\partial\hat{\boldsymbol{R}}}{\partial k_x}\times\frac{\partial\hat{\boldsymbol{R}}}{\partial k_y}\right)\frac{dk_x dk_y}{4\pi} = \mathrm{sgn}(m) \tag{3}$$

Here, the coefficient 2 counts the contributions from the top and bottom surfaces; the integration (carried out over the Brillouin zone, BZ) gives a winding number of one-half for the spin texture shown in FIG. 1c. Thus, the Chern number is one, and its sign is that of the mass term, which depends on the sign of the exchange coupling and on the magnetization direction. Therefore, when E_F is located within the mass gap, the Hall conductivity is quantized, $\sigma_{xy} = \pm\frac{e^2}{h}$ according to the TKNN formula. This implies the emergence of a QAHE, one of the hallmarks of magnetic TIs. The QAHE gives rise to a chiral edge mode (CEM; FIG. 1d), the direction of which depends on the sign of the Chern number and on the magnetization direction.

According to the modern view of the intrinsic AHE in an itinerant ferromagnet[14], spin–orbit coupling often

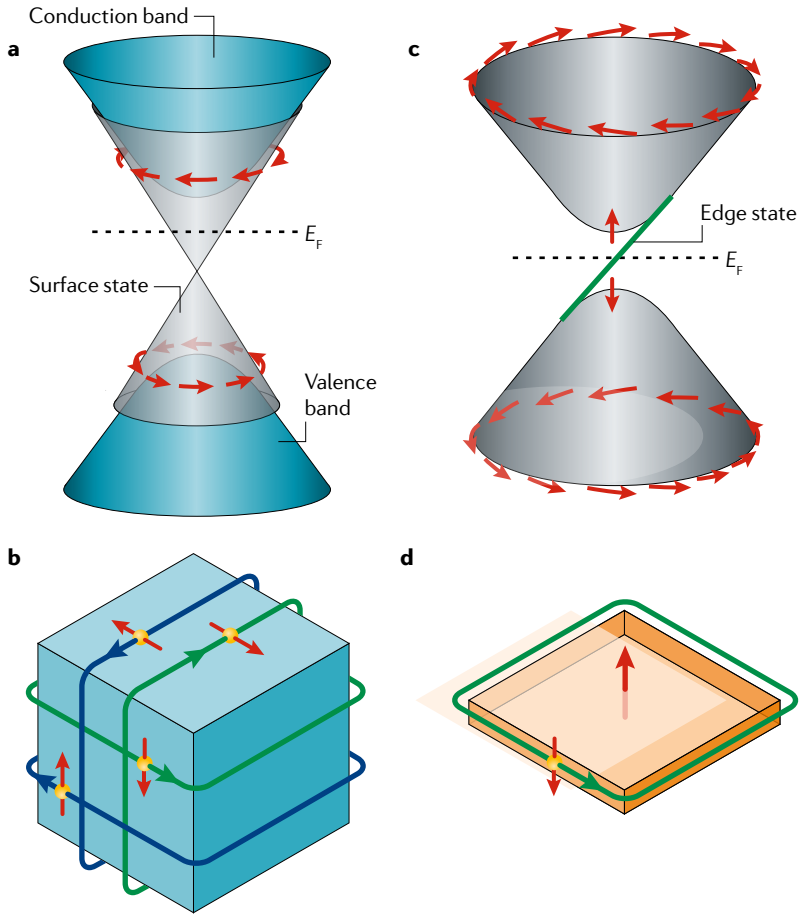

Fig. 1 | **The electronic structure of a topological insulator and of a magnetic topological insulator. a** | The massless Dirac-like dispersion of the surface state with spin–momentum locking in a topological insulator. The surface state band connects the bulk valence and the bulk conduction bands. **b** | Real-space picture of the surface state in a topological insulator. Electrons with spins pointing up and down (red arrows) move in opposite directions. **c** | The gapped Dirac-like dispersion of the surface state in a magnetic topological insulator. **d** | The chiral edge mode that appears in a magnetic topological insulator when the Fermi level, E_F, is located in the mass gap induced by the magnetic exchange interaction. The edge electrons conduct electricity without dissipation in one direction along the edge of the sample.

causes the opening of an anticrossing gap in the spin-polarized band around a specific k-point, while closing it at another k-point, leading to the appearance of Weyl fermions[26–28]. Many anticrossing gaps in momentum space behave as magnetic monopoles in the context of the k-space Berry curvature and hence contribute to the AHE observed in itinerant ferromagnets[14,29]. In this context, the QAHE in magnetic TIs provides the ideal platform for the study of the AHE: a magnetic TI is characterized by a single magnetic monopole in the 2D momentum space, located at $k = 0$ (the Γ point in the first Brillouin zone). The surface state band in magnetic TIs maintains the spin–momentum locking when E_F is located away from the gap region while keeping the spontaneous magnetization. This property of magnetic TIs may bring about versatile spintronic functions, as discussed later.

Several excellent review papers on TIs[4,6,23,24,30] and magnetic TIs[31–33] are available. This Review is focused on recent experimental developments, particularly in the study of CEMs, topological magnetoelectric effects and spintronic functionalities. We start by discussing the methods for the successful realization of magnetic TIs by transition metal elemental doping with a surface state exchange gap. Next, the experimental realization of the QAHE by tuning the Fermi level to the hybridization gap is explained, with a focus on the archetypal material system: $(Bi,Sb)_2Te_3$ doped with transition metals. This explanation is followed by a survey of the emergent phenomena related to the QAHE, such as CEMs and topological magnetoelectric and magneto-optical effects. We also discuss various spintronic functionalities that leverage the spin–momentum locking of the surface state. Finally, we overview the future perspectives for the field, including realization of the QAHE at higher temperatures, the external control of this state and the possible realization of exotic topological states of matter in magnetic TIs.

Origins of magnetism in magnetic TIs

For the emergent properties of magnetic TIs to appear, the formation of the exchange gap in the surface state is essential. The gap is induced by an interaction between the electrons in the surface state and the spontaneous magnetization, as described by the mass term in equation 2; this term is $m\sigma_z \equiv -Jn_S\bar{S}_Z\sigma_Z$, where $\hat{z}$ is the unit vector normal to the surface, J is the exchange coupling between the z component σ_Z of the spin of the Dirac electrons and the localized spin $\boldsymbol{S}$ and n_S is the areal density of localized spins, which have average z component $\bar{S}_Z$ (REF.[18]). The chemical doping with 3d transition metal elements is an effective approach to creating a magnetic interaction with the surface state, as was originally proposed theoretically[17,34–37]. Transition metal doping in TIs owes its success to the knowledge accumulated from studies of diluted magnetic semiconductors[5,38–40].

Two mechanisms have been considered as a possible origin for ferromagnetism in magnetic TIs: the carrier-mediated Ruderman–Kittel–Kasuya–Yosida (RKKY) mechanism[41,42] and the local valence-electron-mediated Bloembergen–Rowland[38,39,43], or Van Vleck[17], mechanism. The role of the RKKY mechanism was experimentally verified in Mn-doped Bi_2Te_3 (REF.[44]), as exemplified by measurements on an electric-double-layer transistor composed of $Mn_xBi_{2-x}Se_yTe_{3-y}$ single crystal flakes ($x = 0.04$ and $y = 0.12$; FIG. 2a,b)[45]. The Hall conductance in this type of sample can be effectively controlled by applying a gate bias V_B; both the amplitude and hysteresis of the Hall conductance are enhanced as the electron density decreases. This behaviour of σ_{xy} reflects a carrier-dependent ferromagnetism (FIG. 2a). The ferromagnetic Curie temperature of the sample, T_C, is dramatically enhanced with the reduction in the electron density, signalling that the ferromagnetism develops progressively as E_F approaches the Dirac point (FIG. 2b). This trend appears to be unexpected in the context of an intuitive understanding of the RKKY mechanism, in which the effective carrier-mediated interaction for the ferromagnetism increases with the carrier density, at least in the relatively low-carrier-concentration region. However, the observation of maximum T_C at the Dirac point can be rationally accounted for in terms of the maximization

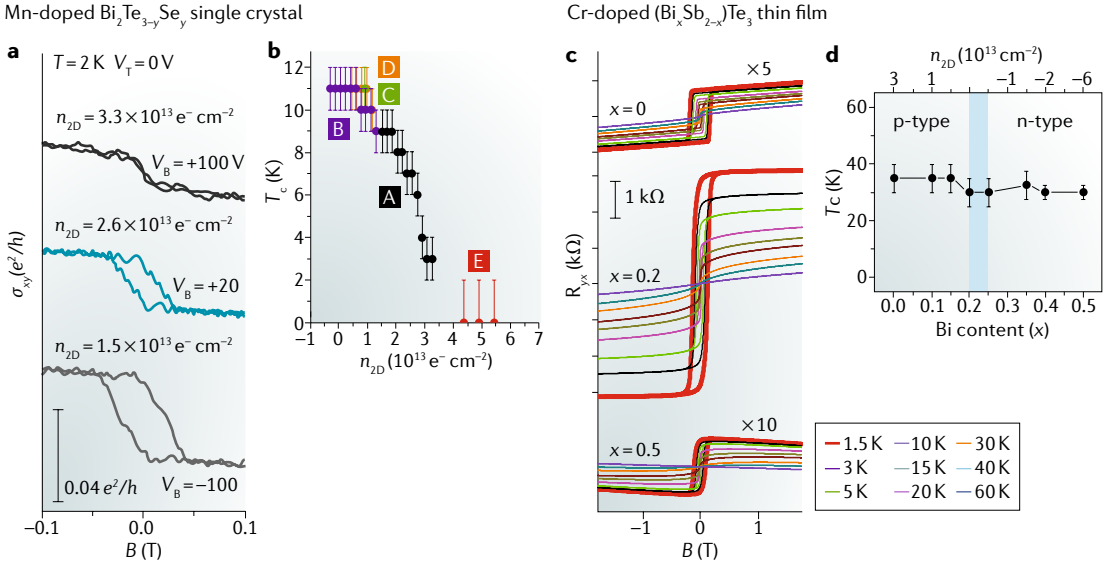

Fig. 2 | **Two possible mechanisms for the ferromagnetism in magnetic topological insulators. a** | The gate bias V_B applied to an electric-double-layer transistor based on $Mn_xBi_{2-x}Se_yTe_{3-y}$ single crystal flakes ($x = 0.04$ and $y = 0.12$) controls the anomalous Hall effect. The temperature $T = 2$ K, σ_{xy} is the Hall conductance, B is the external magnetic field and n_{2D} is the density of charge carriers in the surface state. **b** | Ferromagnetic Curie temperature T_C as a function of n_{2D} for Mn-doped $Mn_xBi_{2-x}Se_yTe_{3-y}$ observed for five samples (A–E) with different carrier densities. **c** | Influence of the Bi content x on the anomalous Hall effect for $Cr_{0.22}(Bi_xSb_{1-x})_{1.78}Te_3$ thin films, measured at various temperatures. **d** | T_C for $Cr_{0.22}(Bi_xSb_{1-x})_{1.78}Te_3$ is plotted as a function of x and charge n_{2D}; the blue region corresponds to the charge neutral point. R_{yx}, Hall resistance. Panels **a** and **b** are adapted from REF.[45], Springer Nature Limited. Panels **c** and **d** are adapted with permission from REF.[47], Wiley-VCH.

of the energy gain of the Dirac electronic system owing to the opening of the exchange gap induced by the ferromagnetism[41], analogously to the Peierls transition that is accompanied by the opening of an electronic gap in electron–lattice coupled systems. The related carrier-mediated ferromagnetism in the surface state is also observed in scanning tunnelling microscopy (STM) experiments[46]. An alternative interpretation is that the change in T_C in gated $Mn_xBi_{2-x}Se_yTe_{3-y}$ may originate from ferromagnetic spin–spin interactions mediated by the bulk valence band[45].

The other mechanism underlying ferromagnetism, mediated by local valence electrons, is the Bloembergen–Rowland, or Van Vleck, mechanism. This kind of ferromagnetism, induced by doping with 3*d* transition metals, is observed, for example, in Cr-doped $(Bi,Sb)_2Te_3$. In 5-nm-thick $Cr_{0.22}(Bi_xSb_{1-x})_{1.78}Te_3$ thin films[47], the coercive field H_C in the hysteresis of the Hall resistance R_{yx} does not depend on the Bi content x (FIG. 2c). Nevertheless, the sign of the ordinary Hall term (the slope of R_{yx} at a high magnetic field) reverses from positive at $x = 0$ to negative at $x = 0.5$, indicating that E_F can be controlled by varying x across the charge neutral point and that E_F is within the exchange gap around $x = 0.2$. The T_C in this system is rather insensitive to the carrier type or charge carrier density (FIG. 2d). This result is in sharp contrast to the carrier-density-dependent T_C for the Mn-doped case (FIG. 2b).

In a theoretical study of the QAHE[17], Van Vleck paramagnetism was proposed as a plausible origin for the ferromagnetism with considerable gain of spin susceptibility owing to the mixing of the conduction and valence bands. Experiments on the QAHE in Cr-doped[16,47] and V-doped[48] 3D TIs supported this idea. In light of the constant T_C, another interpretation based on the Bloembergen–Rowland mechanism[38,39,43] was also put forward. In particular, the ferromagnetic interaction mediated by valence electrons in a narrow-gap semiconductor would explain the results without the need of invoking a large concentration of itinerant conduction carriers[38].

Thus, although the QAHE has been experimentally observed in both Cr-doped and V-doped systems, the microscopic origin of the ferromagnetism remains to be clarified with further theoretical and experimental investigations[49].

The opening of a gap in the surface state has been experimentally verified with surface-sensitive techniques such as spectroscopic-imaging STM (SI-STM)[50] and angular-resolved photoemission spectroscopy (ARPES)[51–53]. Because of the form of the exchange interaction, $-Jn_S\bar{S}_Z\sigma_Z$, the size of the gap is governed by the coupling strength as well as by the effective spin density. The spatial distribution of the exchange gap in a single crystal of $Cr_{0.08}(Bi_{0.1}Sb_{0.9})_{1.92}Te_3$ ($x = 0.08$, $T_C = 18$ K) was characterized at $T = 4.5$ K by SI-STM with quasiparticle interference measurements[50] (FIG. 3a,b). The conductance spectra acquired at different positions on the surface indicate that the gap size ranges between 9 meV and 48 meV (FIG. 3a), and the distribution of the gap sizes is centred around 30 meV (FIG. 3b). The width of the distribution indicates an inherent random distribution of Cr concentration or of the exchange interaction in the crystal. Thus, the improvement in the spatial uniformity of the strength of the exchange interaction plays a vital role in the realization of a large gap in the surface state.

The gap formation has also been observed by ARPES in a Se-rich bulk crystal, $(Bi_{0.84}Fe_{0.16})_2Se_{3.7}$. The exchange

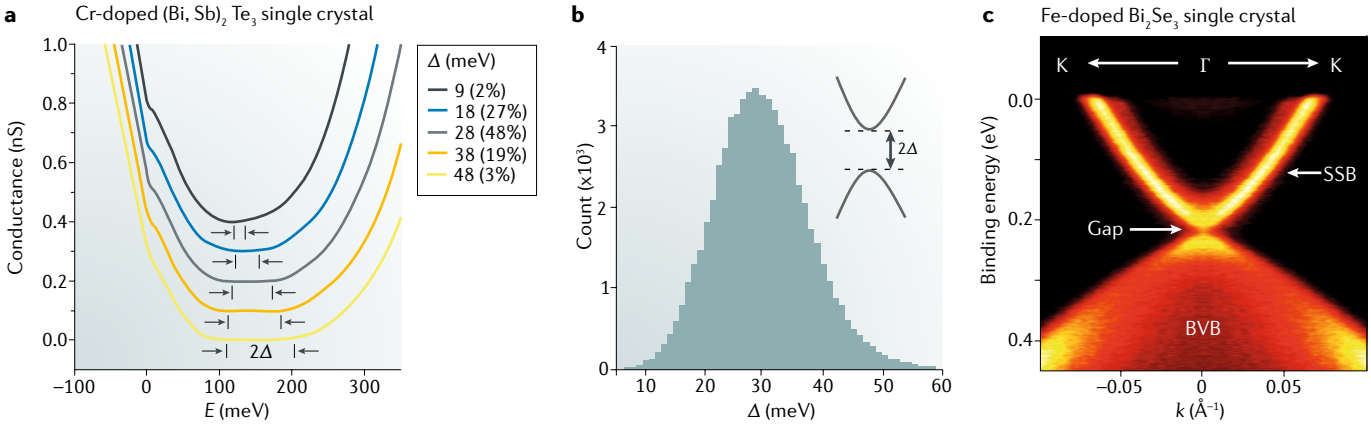

Fig. 3 | **Exchange gap formation by magnetization. a** | Conductance spectra measured by scanning tunnelling spectroscopy at different positions in a $Cr_{0.08}(Bi_{0.1}Sb_{0.9})_{1.92}Te_3$ single crystal. The curves are shifted for clarity. The near-zero-conductance regions between the pairs of arrows correspond to the mass gap and enable evaluating its size, Δ. **b** | Distribution of the gap sizes. **c** | Electronic band structure of a $(Bi_{0.84}Fe_{0.16})_2Se_{3.7}$ crystal (Curie temperature of ~170 K) measured by angular-resolved photoemission spectroscopy. Γ and K, high-symmetry points in the first Brillouin zone; BVB, bulk valence band; *E*, electron energy; *k*, electron momentum; SSB, surface state band. Panels **a** and **b** are adapted with permission from REF.[50], PNAS. Panel **c** is adapted with permission from REF.[51], AAAS.

gap in the crystal surface at $T = 10$ K is observed at the Dirac point of the surface state band[51] (FIG. 3c). The size of the gap, evaluated from the energy distribution curves, is approximately 50 meV and decreases with decreasing Fe concentration. Thus, the exchange interaction between the surface states and the spontaneous magnetization results in the formation of an exchange gap with a size of a few tens of meV.

The experimental verification of the magnetic properties of the samples and the characterization of the exchange gap are essential steps towards the materialization of the QAHE and of the topological magnetoelectric effect in magnetic TIs. A careful consideration of the inhomogeneity of magnetic dopants in terms of microscopic phase segregation, the coexistence of the exchange gap and gapless bands[54] and the impurity bands[55] will be needed to improve the understanding and control over these systems.

Experimental observations of QAHEs

As discussed in the introduction, the QAHE can be intuitively understood as the equivalent of the QHE at zero magnetic field and is characterized by the formation of dissipationless 1D chiral edge conduction channels. The number of quantized states is governed by the topological Chern number, *C*; in the case of the QAHE, there is a one-to-one correspondence between the sign of C ($= \pm 1$) and the magnetization direction. Two prerequisites for the observation of the QAHE are the formation of an exchange gap induced by the coupling with the magnetization in or next to the TI and the precise tuning of E_F into the gap. When E_F is located in the exchange gap, the tangent of the Hall angle, σ_{xy}/σ_{xx}, diverges as a consequence of the quantization of the Hall conductivity $\sigma_{xy} \approx e^2/h$ and the disappearance of the longitudinal conductivity $\sigma_{xx} \approx 0$ owing to the Berry curvature at the exchange gap[14,17]. For the gap to form, the magnetization direction should be along the *z* direction (normal to the surface), which results in the top and bottom surfaces being insulating and the conduction occurring only at the side edge of the surface.

In the theoretical prediction of the QAHE[17], two transition metal elements, Cr^{3+} and Fe^{3+}, were proposed as candidates for magnetic-ion doping. In the first experimental demonstration of the QAHE (FIG. 4a–c), the quantization of the Hall resistance $\rho_{yx} \approx h/e^2$ was measured in a uniformly Cr-doped $(Bi_{1-y}Sb_y)_2Te_3$ (CBST) 5-nm-thick film on a $SrTiO_3$ substrate[16]. ρ_{yx} switches between $+h/e^2$ and $-h/e^2$, accompanying the magnetization reversal resulting from the application of low positive and negative magnetic fields. Two signatures of the QAHE are clearly observed: one is the manifestation of a QHE-equivalent phenomenon even under zero magnetic field, and the other is the chirality reversal of the 1D edge conduction upon reversal of the magnetization direction. By applying a gate voltage V_g via the dielectric substrate to tune E_F, the saturated ρ_{yx} value deviates from the quantized value h/e^2, whereas the coercive field remains constant. There is a narrow V_g region in which the Hall conductance σ_{xy} is quantized and σ_{xx} is nearly zero (FIG. 4c). The small range of values of V_g for which this condition is realized indicates that precise tuning of E_F is crucial to realize the QAHE.

Two years after these measurements on CBST[16], the QAHE was also demonstrated for V-doped $(Bi_{1-y}Sb_y)_2Te_3$ (VBST) 4-nm-thick films on $SrTiO_3$ (FIG. 4d–f). VBST has a larger coercive field (~1 T) than CBST and displays better quantization characteristics, with values closer to $\rho_{yx} \approx h/e^2$ and $\rho_{xx} \approx 0$ at $T = 25$ mK (REF.[56]) (FIG. 4e). At $T = 120$ mK (FIG. 4f), however, ρ_{xx} maintains a finite value, while V_g is tuned to maximize ρ_{yx}, meaning that the residual in-gap states remain at E_F in the exchange gap. Regardless of the relatively high T_C of approximately 20 K for both CBST and VBST with the present transition metal doping level, the temperature at which the full quantization is realized is lower than 100 mK. The temperature at which the QAHE can be observed is several orders of magnitude lower than T_C and the temperature

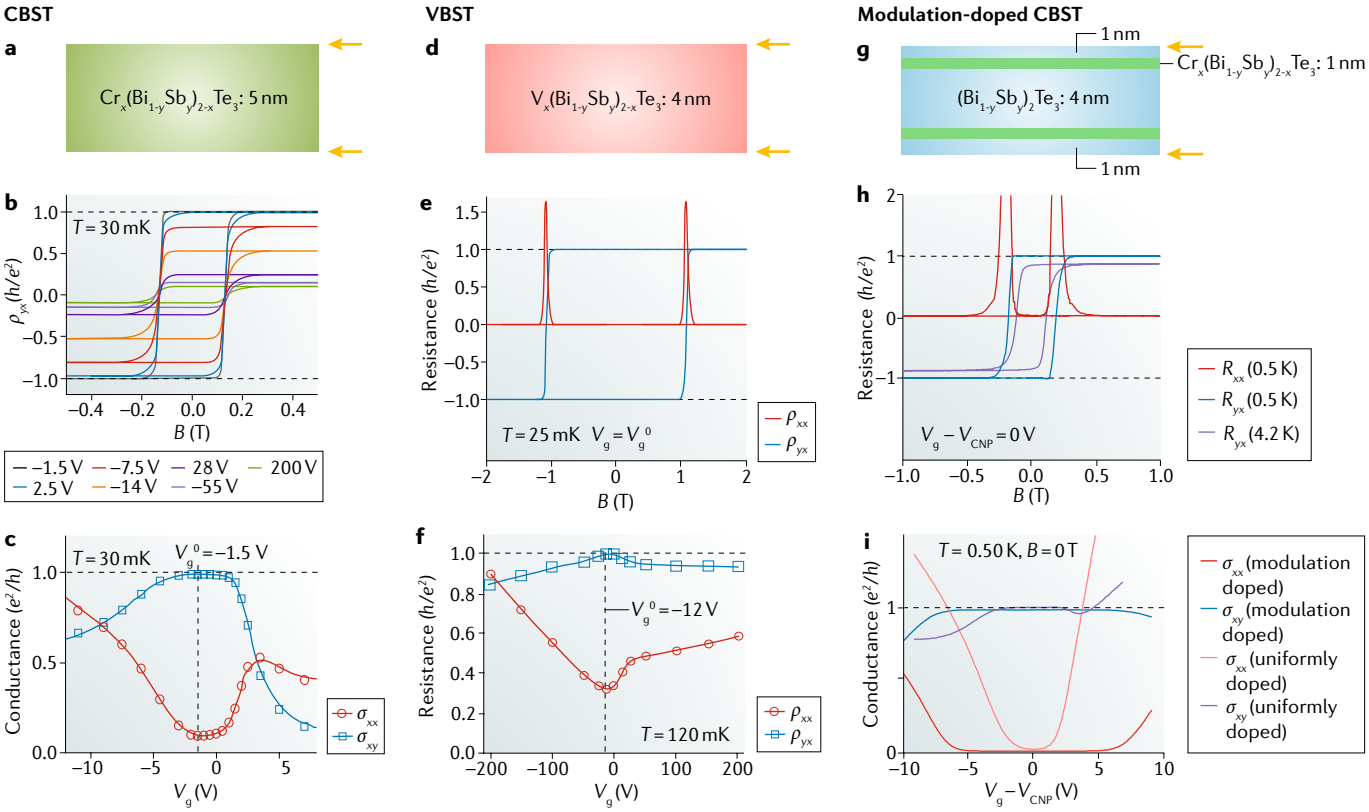

Fig. 4 | **Experimental observations of the quantum anomalous Hall effect. a** | The first observation of the quantum anomalous Hall effect was in a 5-nm-thick film of uniformly Cr-doped $Cr_x(Bi_{1-y}Sb_y)_{2-x}Te_3$ (CBST) grown on a $SrTiO_3$ substrate and measured at 30 mK. Yellow arrows indicate the locations of the surface states at the top and bottom of the film. **b** | Magnetic field (*B*) dependence of the Hall resistance ρ_{yx} for CBST for various gate voltages (V_g). **c** | V_g dependence of the Hall and longitudinal conductance, σ_{xy} and σ_{xx}, respectively, for CBST. **d** | Measurements on a 4-nm-thick uniformly V-doped $V_x(Bi_{1-y}Sb_y)_{2-x}Te_3$ (VBST) film on $SrTiO_3$ at 25 mK. **e** | Magnetic field dependence of the Hall and longitudinal resistance, ρ_{yx} and ρ_{xx}, respectively, for VBST. **f** | Dependence of ρ_{yx} and ρ_{xx} on V_g for VBST at $T = 120$ mK. **g** | Schematic of the Cr-modulation-doped heterostructure on which the measurements in panels **h** and **i** were recorded. **h** | Magnetic field dependence of R_{yx} at 0.5 K and 4.2 K and of R_{xx} at 0.5 K. **i** | Dependence of σ_{xy} and σ_{xx} on V_g for the uniformly doped and modulation-doped CBST at $T = 50$ mK. V_{CNP} is the gate voltage used to tune the charge neutrality point (Dirac point). Panels **b** and **c** are reproduced with permission from REF.[16], AAAS. Panels **e** and **f** are reproduced from REF.[56], Springer Nature Limited. Panels **h** and **i** are adapted from REF.[61], Mogi, M. et al. Magnetic modulation doping in topological insulators toward higher-temperature quantum anomalous Hall effect. *Appl. Phys. Lett.* **107**, 182401 (2015), with the permission of AIP Publishing.

corresponding to the energy of the spectroscopically resolved magnetization gap of the surface state. The large discrepancy likely originates from the presence of dissipative channels, such as nonchiral quasi-helical edge modes[57–59], residual carriers from the bulk valence band[59] and impurity channels formed by defects and magnetic dopants[60], which hinder the dissipationless nature of the chiral edge states.

To improve the observation temperature of the QAHE, a magnetic modulation doping technique was developed. As discussed, the suppression of the inhomogeneity in the distribution of the gap size is a key issue. The QAHE was observed in a modulation-doped heterostructure consisting of five alternating layers of $(Bi_{1-y}Sb_y)_2Te_3$ (BST) and CBST for a total thickness of 8 nm, in which the film thickness and the dopant concentration are precisely controlled[61]. Two magnetic layers with a high Cr concentration of ~20% induce a large exchange coupling to the surface states at the top and bottom BST layers (FIG. 4g). The QAHE is well developed even at $T = 0.5$ K (FIG. 4h), which indicates that disorder is effectively suppressed by the insertion of BST as a main body in the heterostructure. The gapped surface states are located only at the top and bottom surfaces of the heterostructure, as in uniformly doped samples. The robustness of the QAHE in the heterostructure is exemplified by the possibility of tuning E_F using a fairly wide range of values of V_g through the underlying AlO_x dielectric layer (FIG. 4i). A higher-temperature QAHE was also realized in a Cr and V co-doped BST thin film thanks to the improvement in the homogeneity of the ferromagnetism[62].

The Cr-doped, V-doped, (Cr, V)-doped and modulation-doped $(Bi,Sb)_2Te_3$ systems have thus been used to realize the QAHE. The common universality in the QAHE and QHE is verified in terms of the scaling behaviour in the σ_{xy}–σ_{xx} plot[59,63–65], the quantum Hall breakdown at large current density[66,67] and the criticality of the quantum Hall plateau transition[68], even though the microscopic origins of the quantization

are quite different: the gap opens at E_F because of the exchange coupling with the spontaneous magnetization for the QAHE, whereas it is the result of the formation of Landau levels originating from the cyclotron motion of 2D charge carriers for the QHE. The QAHE in other candidate materials, such as $(Bi,Sb)_2Te_3$ or Bi_2Se_3 doped with other 3*d* transition metals[17] and Mn-doped HgTe (REF.[69]), although identified theoretically, has not yet been experimentally realized. However, the observation of the QAHE in different materials is highly desirable to further study its unconventional characteristics and to pursue its observation at higher temperatures.

One possible application of the QAHE would be the electrical resistance standard, in analogy to the QHE[70]. Because the QAHE can be realized at zero or very low magnetic fields, it would be easier to use as a reference compared with the QHE, which requires high magnetic fields. Moreover, the quantization of the conductance at zero magnetic field, combined with a Josephson device, may produce a new type of quantum metrology[71]. Presently, the uncertainty of the resistance in QAH systems (V-doped[72] and Cr-doped[67] BST) has been reported to be ~0.2–1 part per million, as characterized with a cryogenic current comparator bridge technique. These values are still three or four orders of magnitude worse than those for GaAs/AlGaAs (REF.[73]) and graphene[74]. Further improvement of the uncertainty is linked to the realization of the QAHE at higher temperatures and to its robustness against large current injection, which can be achieved through the development of less-disordered QAHE samples and improved device configurations.

Chiral edge conduction

As discussed, the QAH state is topologically characterized by a Chern number that is $C = +1$ or $C = -1$ when the magnetization points upwards or downwards, respectively. This feature enables the control and manipulation of the physical properties of the chiral edge conduction channels, for example, the edge conduction at magnetic domain walls and the formation of chiral Majorana edge modes, as argued in the following. At the interface between the magnetic TI and a vacuum, the Chern number changes from $C = \pm 1$ to $C = 0$ such that one CEM appears at the sample edge. By contrast, when the magnetization changes from downward to upward across a magnetic domain wall, the Chern number changes from $C = -1$ to $C = +1$, and two CEMs co-propagate along the domain wall[6,7,18,75] (FIG. 5a). The presence of CEMs at domain walls is experimentally supported by transport measurements performed in the multidomain state at the magnetization reversal[45,76]. In one experiment, increased conductivity was observed in the multidomain state and was attributed to the formation of dissipationless conduction at the domain wall[45]. In another experiment, a discrete jump in the longitudinal and Hall resistance, as large as ~0.1 h/e^2, was observed, accompanied by the formation of a large magnetic domain wall and chiral edge conduction[76]. Afterwards, CEMs were observed on a single domain wall in an experiment that used the tip of a magnetic force microscope to write domains[77]. In this technique, the magnetization direction is locally reversed by scanning over the sample owing to the stray magnetic field from the magnetized tip. Thus, the position of the domain wall can be continuously changed by moving the tip (FIG. 5b). This technique was applied to study transport in a modulation-doped CBST film at 0.5 K in a Hall bar configuration[77] (FIG. 5c). Initially, the magnetization points downwards, and a single domain exists; moreover, the Hall (R_{13} and R_{24}) and longitudinal (R_{12} and R_{34}) resistance values are $-h/e^2$ and 0, respectively. When the magnetic domain wall is in between the contacts, the Hall resistance on the left side, R_{13}, is $\sim+h/e^2$, whereas R_{24} is $\sim-h/e^2$, owing to a magnetization reversal only on the left-hand side, as expected. Regarding the longitudinal resistance, R_{12} takes a high resistance value of $\sim 2h/e^2$, whereas R_{34} remains at almost zero. These resistance values are nothing but the evidence of the presence of CEMs along the domain wall. As the two CEMs co-propagate along the domain wall, they intermix and equilibrate with each other, and the electrons are finally equally distributed downstream of point D, which lies in between contacts 3 and 4. Consequently, R_{34} becomes zero because the potentials downstream are equal. By contrast, R_{12} assumes a value that is twice the quantized resistance, $2h/e^2$, because only half of the electrons injected from current contact 5 would be ejected to the other current contact, that is, 6 (REF.[78]). Finally, when the magnetization direction is completely reversed by the tip, the Hall and longitudinal resistance values recover the quantized values for an upward-pointing domain with $C = +1$. The presence of CEMs at the domain wall was also confirmed by another experiment, in which the Meissner effect in a superconductor was used to shield the external magnetic field and obtain the desired magnetic domain structure[79]. Although the basic characteristics of CEMs are expected to be almost identical between the sample edge and domain walls, the high controllability of domain walls enables the construction of dissipationless and reconfigurable circuits. In fact, proof-of-concept CEM circuits were demonstrated, exploiting the unique chiral nature of CEMs[77,79].

An even more exotic CEM can be realized by leveraging the superconducting proximity effect on the QAHE. It was proposed that the superconducting proximity effect on a TI results in the formation of a topological superconductor, accompanied by the appearance of Majorana fermions at vortex cores or at the sample edge[6,7,80–82]. Majorana particles, which were originally introduced in the context of high-energy physics, are fermions that are their own antiparticles[83]. The realization of Majorana fermions as composite particles in condensed matter should enable non-Abelian braiding operations in topological quantum computations, which would then be robust against local perturbations[84–86]. One experimental approach to the realization of Majorana quasiparticles exploited a junction between a superconductor, Nb, and a magnetic TI[87] (FIG. 5d). The topological superconductor is characterized by a Bogoliubov–de Gennes (BdG) Chern number *N*, which is defined in the BdG Hamiltonian with particle–hole symmetry[82]. When the proximitized superconducting gap Δ at the top surface of the TI, the surface adjacent to Nb, is larger than the magnetization gap $|m|$, a topological superconducting state is stabilized, and the BdG Chern number becomes $N = \pm 1$. By contrast,

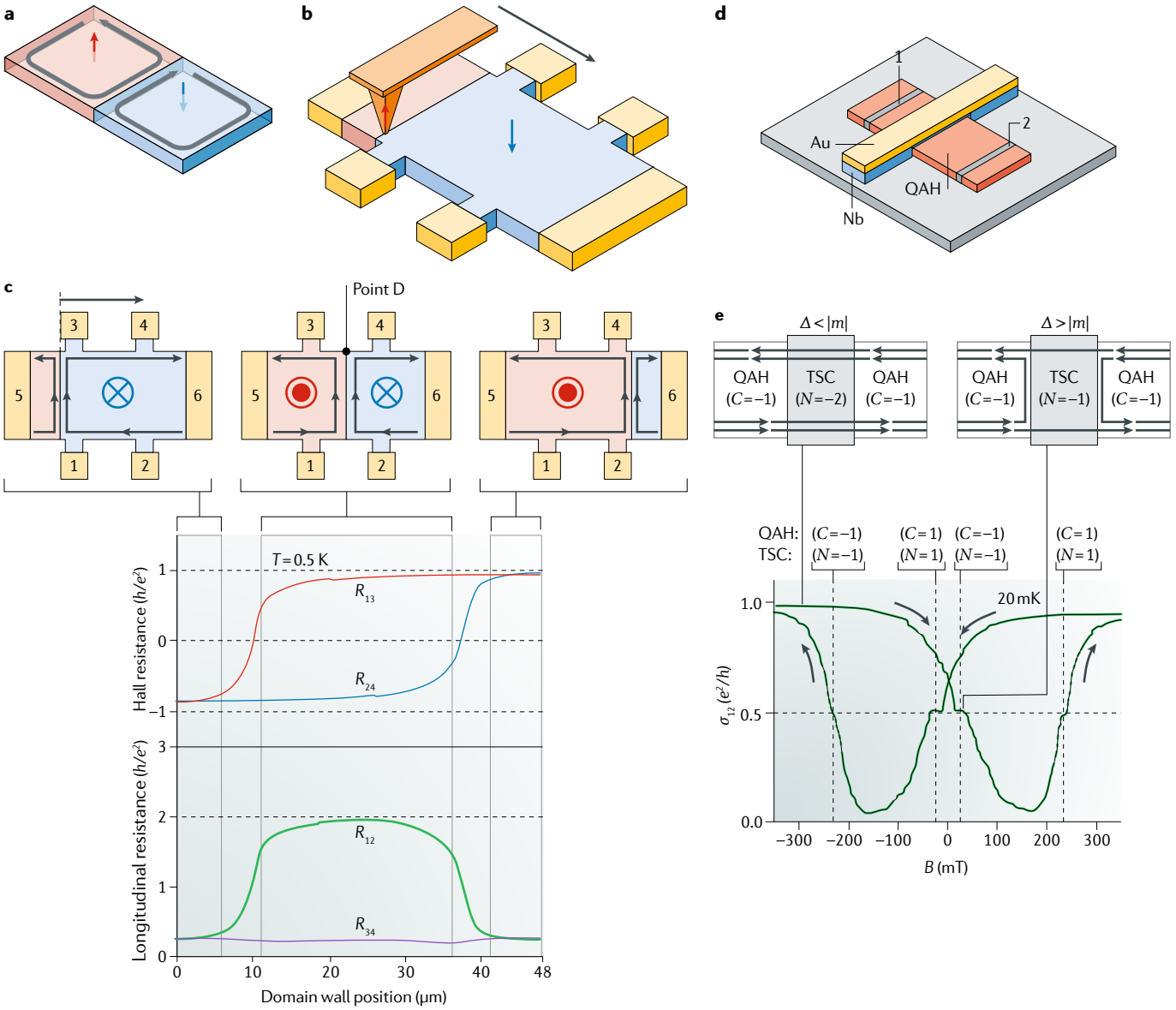

Fig. 5 | **Chiral edge conductions. a** | Schematic illustration of chiral edge conduction along a domain wall of a magnetic topological insulator in the quantum anomalous Hall (QAH) state. Two chiral edge modes appear at the boundary between the domain with magnetization pointing upwards and that with magnetization pointing downwards. **b** | Schematic drawing of the measurement procedure for studying the dependence of the transport properties on the domain wall position using a magnetic force microscope (MFM). The domain wall position is continuously moved from left to right, following the scan over the sample with the MFM tip. **c** | Variation of the Hall resistances, R_{13} and R_{24}, and longitudinal resistances, R_{12} and R_{34}, measured during continuous MFM tip scanning from left to right on the Hall bar. The schematics in the upper panel illustrate the domain configurations of the Hall bar at the three relevant regions. Point D represents the downstream point on the domain wall. **d** | Schematic illustration of the measurement procedure for detecting chiral Majorana edge modes at the boundary between a QAH state and a superconductor, Nb, in a QAH–topological superconductor (TSC) device. **e** | The dependence on the magnetic field (B) of the longitudinal conductivity σ_{12}. A half-quantized conductance plateau is observed at the magnetization reversal point. The schematics in the upper panel illustrate the edge transport configurations for $C = -1$, $N = -2$ and $C = -1$, $N = -1$. Δ, superconducting gap; C, topological Chern number; $|m|$, magnetization gap; N, Bogoliubov–de Gennes Chern number; T, temperature. Panels **a**, **b** and **c** are reproduced with permission from REF.[77], AAAS. Panels **d** and **e** are adapted with permission from REF.[87], AAAS.

when $\Delta < |m|$, a QAH state is realized, and the BdG Chern number is related to the Chern number, with the relation $N = 2C = \pm 2$. In this measurement, the chiral Majorana edge mode, which can be interpreted as a 1D propagating Majorana fermion, is expected to appear at the interface between phases with different BdG Chern numbers. Note that one CEM in the QAH state can be interpreted as two co-propagating chiral Majorana edge modes; in other words, one chiral Majorana edge mode corresponds to half a CEM. The magnetic field dependence of the two-terminal conductivity σ_{12} of the sample is shown in FIG. 5e. The mass gap m is expected

to continuously change from negative to positive as a result of the magnetization reversal[64,88,89]. As a result, a sequential topological phase transition from a QAH state to a topological superconducting state is induced by the magnetic field. Initially, when the magnetization points downwards, Δ is smaller than $|m|$; hence, $C = -1$ and $N = -2$, and the two-terminal conductance σ_{12} is quantized to e^2/h. When $|m|$ becomes smaller than Δ at the magnetization reversal point as the magnetic field is swept, a single chiral Majorana edge mode is formed at the boundary between the QAH state ($C = -1$, $N = -2$) and the topological superconductor ($N = -1$; FIG. 5e). In this situation, one of the two chiral Majorana edge modes is reflected back to the current terminal, while the other propagates along the edge of the sample. The splitting leads to a half quantization of the conductance, $e^2/2h$, which is observed as a half-quantized plateau[87]. Although the interpretation of the half-quantized plateau appearing in σ_{12} is still controversial[90–92], the solid confirmation of chiral Majorana edge modes would enable non-Abelian braiding and topological quantum computation in the future[93].

Topological magnetoelectric effects

Aside from their topologically protected surface state, TIs also exhibit bulk magnetoelectricity[94]. Indeed, the topological band inversion brings about an important modification of Maxwell's equation. In TIs, the application of a magnetic field induces an electric polarization, whereas an electric field induces a magnetization. This is the magnetoelectric effect, which is characterized by a coefficient quantized to the fine structure constant. The experimental observation of the quantized magnetoelectric response is especially important from a fundamental point of view, because measuring the quantized magnetoelectric response corresponds to a direct measurement of the Z_2 invariant through a response function. Developments in the heterostructure engineering of magnetic TIs and the establishment of terahertz measurement techniques enabled the direct observation of this effect.

To describe the electromagnetic response in a TI, a Lagrangian[94] was derived that includes, in addition to the conventional Maxwell term, the so-called axion term L_{TI},

$$L_{\mathrm{TI}} = \frac{\theta e^2}{2\pi h}\boldsymbol{E}\cdot\boldsymbol{B} = \sqrt{\frac{\varepsilon_0}{\mu_0}}\,\alpha\frac{\theta}{\pi}\boldsymbol{E}\cdot\boldsymbol{B} \tag{4}$$

$$\theta = -\frac{1}{4\pi}\int_{\mathrm{BZ}} d^3k\,\varepsilon_{ijk}\,\mathrm{Tr}\left[a_i\partial_j a_k - i\frac{2}{3}a_i a_j a_k\right] \tag{5}$$

where $\alpha(=\frac{1}{2\varepsilon_0}\frac{e^2}{hc}\approx 1/137)$ is the fine structure constant and ε0 and μ0 are the permittivity and permeability of free space, respectively. $a_i^{\mu\nu}(=i\langle u_{\mu\boldsymbol{k}}|\frac{\partial}{\partial k_i}|u_{\nu\boldsymbol{k}}\rangle)$ is the Berry connection, and $|u_{\nu\boldsymbol{k}}\rangle$ is the lattice-periodic part of the Bloch function for the occupied band ν; the trace is taken over the occupied bands, and the integration is carried out within the Brillouin zone. Interestingly, LTI takes the same form as the term describing axion electrodynamics in quantum chromodynamics[95]. Under time-reversal symmetry, θ is equal to π (mod 2π) within the TI and zero in a vacuum or in an ordinary insulator. When time-reversal symmetry is broken under the presence of a magnetic field or magnetization, the opening of the gap in the surface state allows a change in θ, producing the exotic electromagnetic responses described below.

The conjunction of the axion term with the Maxwell term leads to the extended Maxwell equation, and the following cross relation between the electric polarization $\boldsymbol{P}$ and magnetic field $\boldsymbol{B}$ and the magnetization $\boldsymbol{M}$ and electric field $\boldsymbol{E}$ can be derived[96]

$$\boldsymbol{P} = \frac{e^2}{2h}\frac{\theta}{\pi}\boldsymbol{B} = \sqrt{\frac{\varepsilon_0}{\mu_0}}\,\alpha\frac{\theta}{\pi}\boldsymbol{B} \tag{6}$$

$$\boldsymbol{M} = \frac{e^2}{2h}\frac{\theta}{\pi}\boldsymbol{E} = \sqrt{\frac{\varepsilon_0}{\mu_0}}\,\alpha\frac{\theta}{\pi}\boldsymbol{E} \tag{7}$$

This represents the magnetoelectric effect[97]. This kind of axion-type coupling, represented by the $\boldsymbol{E}\cdot\boldsymbol{B}$ term in the Lagrangian, and the resultant diagonal magnetoelectric susceptibility are observed broadly in magnetoelectric materials, such as Cr_2O_3 (REF.[98]) and $(Fe,Zn)_2Mo_3O_8$ (REF.[99]). The uniqueness of TIs lies in the fact that the magnetoelectric susceptibility is quantized in units of the fine structure constant α.

The axion term L_{TI} causes an essential modification of Maxwell's equations and a peculiar electromagnetic response called axion electrodynamics. The electromagnetic response of a TI with a surface or interface in contact with a vacuum or with a trivial material ($\theta = 0$) is determined by the boundary conditions. To be realistic, let us consider a magnetic TI thin film and its top and bottom surfaces. When E_{F} lies within the exchange gap, the surface non-dissipative current is expressed as the sum of the polarization current ($\partial_t\boldsymbol{P}$) and magnetization current ($\nabla\times\boldsymbol{M}$); $\boldsymbol{j} = (e^2/2h)\cdot\nabla(\theta/\pi)\times\boldsymbol{E}$. The rotation direction (clockwise or anticlockwise) of θ when going from the vacuum to the TI or vice versa depends on the sign of the mass gap or, equivalently, on the magnetization of the top or bottom layer. Because the magnetizations of the top and bottom surfaces are parallel, $\nabla\theta$ can be additive (2π); hence, $\theta = 0\rightarrow\pi$ (through the top surface) and $\theta = -\pi\rightarrow 0$ (through the bottom surface). This results in the QAHE observed in a thin film with parallel magnetizations on the top and bottom surfaces and gives rise to the quantized Faraday or Kerr rotation of incident electromagnetic waves[100–104], which corresponds to the measurement of the magnetoelectric susceptibility of the TI[105].

A schematic representation of the magneto-optical effects in the QAH state is shown in FIG. 6a. Magneto-optical effects include the Faraday rotation, the rotation of the linear polarization of the transmitted light, and the Kerr rotation, the rotation of the polarization of the reflected light. To probe quantized magneto-optical effects, the photon energy of the incident light has to be tuned below the exchange gap of the surface state

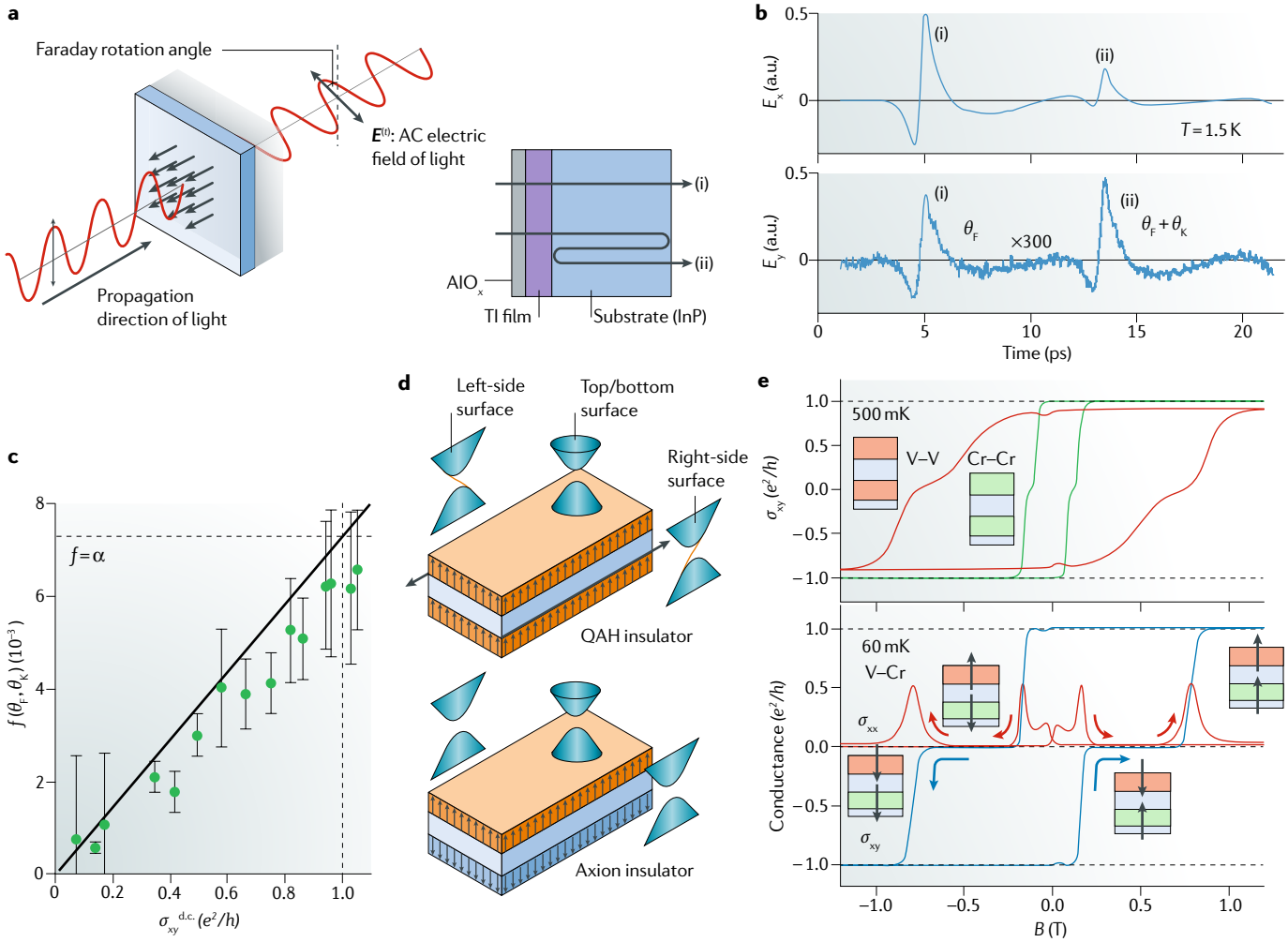

Fig. 6 | **Topological magneto-optical effect and magnetoelectric axion insulator. a** | Schematic of a Faraday rotation measurement for a quantum anomalous Hall (QAH) state. The multiple reflection of terahertz light within the substrate (insulating InP) on which the magnetic topological insulator (TI) film is grown is shown in the right panel; the beam can either go directly through the sample (i) or be reflected from the substrate–vacuum and TI–substrate interfaces (ii). **b** | Temporal profiles of the terahertz light pulses. The upper panel shows the *x* component of the electric field *E*, which coincides with the polarization of the original incident light; the lower panel shows the *y* component of *E*, generated as a result of the polarization rotation. Hence, the (i) and (ii) pulses in E_y contain the Faraday rotation (θ_F) and the Faraday rotation plus Kerr rotation ($\theta_F + \theta_K$), respectively. **c** | The values of the scaling function $f(\theta_F, \theta_K) = \frac{\cot\theta_F - \cot\theta_K}{\cot^2\theta_F - 2\cot\theta_F\cot\theta_K - 1}$ obtained from the experimentally observed θ_F and θ_K values are plotted against the direct current values of the Hall conductivity, $\sigma_{xy}^{d.c.}$. The scaling function value is expected to reach the fine structure constant α when quantization is realized in the QAH state. With decreasing temperature (*T*), σ_{xy} increases, approaching the quantized value of e^2/h, and *f* approaches α. **d** | The upper schematic shows a QAH state with parallel magnetization directions on the top (V-doped) and bottom (Cr-doped) magnetic layers; the lower schematic shows an axion insulator state with antiparallel magnetization on those layers. **e** | The top panel shows the magnetic field dependence of σ_{xy} at 500 mK for symmetric modulation-doped heterostructures with V (pink) and Cr (green). The lower panel shows σ_{xy} and σ_{xx} at 60 mK for V-doped and Cr-doped heterostructures. The insets show the magnetization configuration at each magnetic field (*B*). The antiparallel magnetization configuration realizes an axion insulator state. Panels **a** (right), **b** and **c** are adapted from REF.[102], CC-BY-4.0. Panels **d** and **e** are adapted with permission from REF.[109], AAAS.

of the magnetic TI; otherwise, the surface state or bulk interband transitions would cause dissipation owing to the real excitation of particles and holes. Thus, terahertz light, with a photon energy around a few meV, can be a good probe, and time-domain spectroscopy on thin films grown on thick substrates is powerful for deducing both the Faraday rotation (θ_F) and Kerr rotation (θ_K) simultaneously by using the time delay of the light pulse multiply reflected within the substrate with respect to the pulse going directly through the sample. Results for a Cr-modulation-doped $(Bi,Sb)_2Te_3$ film near the QAH state at 1.5 K are shown in FIG. 6b,c (REF.[102]). The comparison of the time profile of the transmitted light beam for the E_x and E_y polarizations with respect to the purely E_x-polarized incident beam gives the rotation angles (θ_F and θ_K) as the ratio of E_y/E_x (FIG. 6b). The pulse profiles (i) and (ii) represent the directly transmitted beam and the multiply reflected beam, respectively;

therefore, the E_y profile contains contributions from (i) of θ_F and from (ii) of $\theta_F + \theta_K$. Rotations on the order of several milliradian are readily visible despite the magnetic TI films being as thin as 8 nm, which indicates the very large magnitude of the magneto-optical effect in the surface states. The transmission spectra in the terahertz region, as obtained from the Fourier transformation of the time-domain profile, show no appreciable electronic absorption, as expected from the presence of the large exchange gap in the QAH state. By using only the θ_F and θ_K values, we can establish the relation $f(\theta_F, \theta_K) = \alpha$ in the QAH state. Here, f is a scaling function of θ_F and θ_K that depends only on the experimental configuration but contains no material parameters, such as the thicknesses and dielectric constants (refractive indices) of the magnetic TI film and substrate[101,102]; for the present case,

$$f(\theta_F, \theta_K) = \frac{cot\theta_F - cot\theta_K}{\cot^2\theta_F - 2cot\theta_F cot\theta_K - 1}.$$

The variations of the experimentally obtained $f(\theta_F, \theta_K)$ values at various temperatures, plotted against the corresponding direct current values of Hall conductivity σ_{xy}, are shown in FIG. 6c. As σ_{xy} approaches the quantized value (e^2/h) with decreasing temperature (lowest at 1.5 K), $f(\theta_F, \theta_K)$ approaches the value of α, thus confirming the near quantization of the topological magneto-optical effect near the QAH state.

The topological magneto-optical effect is one manifestation of axion electrodynamics. However, in the case of a QAH insulator, the θ term has opposite signs on the top and bottom surfaces. Hence, macroscopically, the topological magnetoelectric effect is cancelled out. To produce a topological (near-quantized) magnetoelectric effect or an axion insulator, it is necessary to realize an antiparallel magnetization (M) or an opposite sign of the exchange gaps on the top and bottom surfaces[106,107]. This is possible using the magnetic modulation doping technique to grow the TI film[108–110] (FIG. 6d). The QAH effect observed for V-doped and Cr-doped $(Bi,Sb)_2Te_3$ TI films is shown in FIG. 6e (top panel); both samples show the quantization of $\sigma_{xy} = \pm\frac{e}{h}$, but they display different coercive forces (B_c), as seen in the different hysteresis curves[16,56]. When a modulation-doped film composed of a large-B_c V layer on top and a small-B_c Cr layer on the bottom is used, a state with M pointing up on the top surface and down on the bottom surface (or vice versa) is realized within the wide hysteresis region[109] (FIG. 6e, bottom panel). Remarkably, such a state is characterized by a zero Hall plateau with zero conductance, which characterizes the axion insulator state, but is distinct from the trivial insulator with $\theta = 0$. In particular, the topological transition between a QAH insulator and an axion insulator is marked by the on–off switching of the chiral edge channel. The two-terminal resistance R_{2T} of the thin-film sample under discussion shows magnetic field switching between $h/e^2 \approx 25.8$ kΩ (irrespective of the sample length) and a high resistance value ($R_{2T} > 10^8$ Ω)[109]. In this state, the topological magnetoelectric effect, manifested as $P_z \approx \sqrt{\frac{\varepsilon_0}{\mu_0}}\alpha B_z$ and $M_z \approx \sqrt{\frac{\varepsilon_0}{\mu_0}}\alpha E_z$, can be expected[106,107] and could be measured using the nonreciprocal polarization rotation — termed gyrotropic birefringence — of terahertz light, as was demonstrated for multiferroics[99].

Spintronic functionalities

In addition to giving rise to QAH-related phenomena, the interaction between spontaneous magnetic moments and spin–momentum-locked conduction electrons in the surface state leads to versatile spintronic functionalities. Magnetic control of the electronic state or electric control of the magnetization is enabled via charge-to-spin conversion by the Rashba–Edelstein effect[111]. The application of an in-plane electric field shifts the Fermi surface in momentum space and causes the accumulation of net spins in the direction perpendicular to that of the current because of the spin–momentum locking at the surface state of the TI. Studies on spin-torque ferromagnetic resonance and spin pumping highlighted the high efficiency of interfacial charge-to-spin conversion $q_{ICS} = J_S^{3D}/J_C^{2D}$ (with J_S^{3D} being the spin current density (A m^{-2}) and J_C^{2D} being the surface charge current density (A m^{-1}))[112], which corresponds to a spin Hall angle θ_{CS} of order unity, assuming an ~1-nm-thick surface state layer[113–121]. The spin Hall angle is much larger for TIs than for heavy metallic elements such as Pt, β-Ta and β-W, which makes TIs an attractive arena to explore unprecedented spintronic functions[123]. Furthermore, the Dirac dispersion of the surface state provides an additional knob to regulate the charge-to-spin conversion efficiency by controlling the Fermi level through composition tuning and/or gate voltage[112,124,125].

One representative example of such spintronic functionalities is the nonlinear unidirectional magnetoresistance[126–130]. When the magnetization of the magnetic TI points along the in-plane direction (y direction), perpendicular to the in-plane current (x direction), the value of the resistance depends on the magnitude and direction (positive or negative) of the applied current. This is phenomenologically understood in terms of the spin accumulation through the Rashba–Edelstein effect: the value of the resistance depends on the direction in which spin moments accumulate, either parallel or antiparallel to the magnetization direction (FIG. 7a), as is the case for the current-in-plane giant magnetoresistance in ferromagnetic/non-magnetic/ferromagnetic heterostructures[131,132]. However, differently from giant magnetoresistance, unidirectional magnetoresistance is a current-nonlinear effect, because the magnitude of the spin accumulation is proportional to the current. The in-plane magnetic field dependence of the longitudinal resistance R_{xx}^{nl} measured under a DC current of +2 μA and −2 μA for a heterostructure composed of a magnetic TI/non-magnetic TI, $Cr_x(Bi,Sb)_{2-x}Te_3/(Bi,Sb)_2Te_3$, is shown in FIG. 7a. In this heterostructure, only the top surface interacts with magnetic moments; hence, cancellation due to opposite contributions from the top and bottom surfaces is avoided[133]. The magnetization points in the out-of-plane direction at 0 T owing to the magnetic anisotropy, but it points in the in-plane direction at 1 T, causing a resistance drop resulting from the closing of the gap of the surface state. A difference

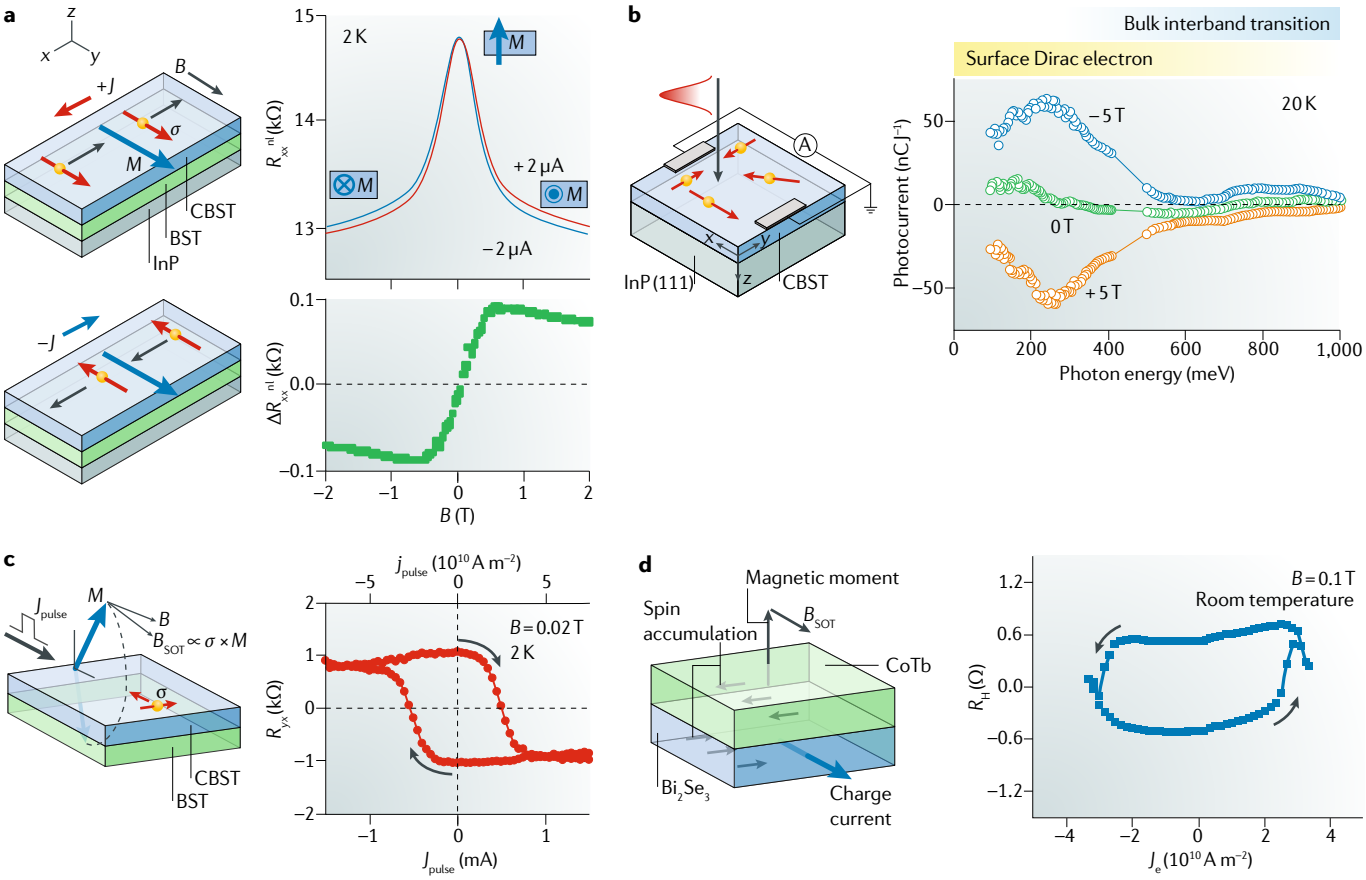

Fig. 7 | **Spintronic functionalities. a** | Schematic setup for the measurement of the nonlinear unidirectional magnetoresistance. $+J$ and $-J$ indicate the current direction; the red and blue arrows labelled σ and M represent the spin accumulation direction and magnetization direction, respectively. The black arrows represent the direction of movement of the surface electrons. The top graph shows the resistance R_{xx}^{nl} of the magnetic topological insulator (TI)/non-magnetic TI heterostructure measured with positive (+2 μA) and negative (−2 μA) DC current under the in-plane magnetic field (B). The lower graph shows the difference between the two resistance curves, ΔR_{xx}^{nl}. **b** | Schematic experimental setup for measuring the photocurrent and zero-bias photocurrent spectra under an in-plane magnetic field of 5 T, 0 T and −5 T. The red arrows represent the electron spin. **c** | Schematic illustration of current-induced magnetization switching in a magnetic TI/non-magnetic TI heterostructure. J_{pulse} is the current pulse, and B_{SOT} is the effective field generated by the spin–orbit torque. The dependence of Hall resistance R_{yx} on the current pulse amplitude J_{pulse} at $T = 2$ K under a small in-plane magnetic field of $B = 0.02$ T, which is required to determine the switching direction, is shown in the graph on the right. The corresponding current pulse density j_{pulse} is shown along the upper axis. **d** | Schematic illustration of the measurement procedure for the room temperature current-induced magnetization switching in a TI/ferromagnetic heterostructure (Bi_2Se_3/CoTb). The dependence of the Hall resistance R_H on the estimated current density J_e inside the Bi_2Se_3 layer is measured under a small in-plane magnetic field of 0.1 T. BST, $(Bi,Sb)_{2-x}Te_3$; CBST, $Cr_x(Bi,Sb)_{2-x}Te_3$. Panel **a** is adapted with permission from REF.[129], APS. Panel **b** is reproduced from REF.[134], CC-BY-4.0. Panel **c** is adapted with permission from REF.[148], APS. Panel **d** is adapted with permission from REF.[151], APS.

in resistance for positive and negative currents, ΔR_{xx}^{nl}, is clearly discerned (FIG. 7a), and it changes sign with the magnetization reversal. Thus, this effect can be exploited to perform an electrical reading of the magnetization direction using a device with a two-terminal geometry, similar to giant magnetoresistance[126–128]. The value of the unidirectional magnetoresistance in magnetic TIs is 10^2–10^6 times larger than that for normal-metal/ferromagnetic-metal heterostructures such as Pt/Co[126–129]. Furthermore, gate tuning of the Fermi level around the Dirac point resonantly enhances ΔR_{xx} (REF.[129]). The microscopic process underlying such a large unidirectional magnetoresistance in magnetic TIs is ascribable to the magnon-mediated backward scattering of the surface state electrons, which would be forbidden in the absence of magnetization. Because of the conservation of angular momentum in the spin–momentum-locked state, electrons with momentum $+k$ and $-k$ are scattered through processes of magnon creation and annihilation, respectively. This situation leads to a difference in the lifetimes of right-moving and left-moving electrons and thus to the difference in the resistance for positive and negative currents: the electron–magnon scattering is asymmetric[129]. The same mechanism likely results in the overestimation of the spin Hall angle in magnetic TIs in a second-harmonic Hall measurement[121,124,148].

A related phenomenon is observed by optical excitation. Under the in-plane magnetization, mid-infrared

photoexcitation induces a zero-bias photocurrent that flows in plane, perpendicular to the magnetization direction[134]. The photocurrent direction depends on the magnetization direction (positive or negative; FIG. 7b). The photocurrent spectra show a maximum at around 250 meV, below the bulk bandgap of the TI (~300 meV, FIG. 7b), meaning that it is the surface Dirac electrons that mainly contribute to the observed photocurrent. The origin of the photocurrent is attributed to the magnetization-induced modification of the energy dispersion resulting from spin–momentum locking plus the parabolic k^2-term. Because of the asymmetric band dispersion for $+k$ and $-k$, both the excitation and relaxation of photoexcited electrons are asymmetric, which yields the zero-bias photocurrent. A shift current process or the presence of a photo-induced Floquet state may also contribute to the photocurrent, as was recently found in polar semiconductors[135,136]. A similar phenomenon is observed in non-magnetic TIs using obliquely incident circularly polarized light instead of the magnetization: this is the circular photogalvanic effect, which points to the possibility of achieving the optical generation of spin currents in TIs[137,138].

The presence of the topological surface state supports the formation of nontrivial magnetic structures in ferromagnetic TIs and related heterostructures. The Dzyaloshinskii–Moriya interaction or the asymmetric exchange interaction between the localized magnetic moments is mediated by the surface state of the TI. Similarly to the interface of non-magnetic/ferromagnetic heterostructures[139], the Dzyaloshinskii–Moriya interaction favours a noncolinear spin ordering and the formation of magnetic skyrmions, which are detected through the topological Hall effect[122,140,141].

One other interesting spintronic phenomenon is the current-induced switching of the magnetization[142–145]. Efficient current-induced magnetization switching is highly desirable for the application of spintronic devices such as magnetic random access memories. As mentioned earlier, current injection in a TI induces a spin accumulation at the surface by the Rashba–Edelstein effect. The angular momentum of the accumulated spin is transferred to the local magnetization, m, which causes the damping-like spin–orbit torque (Slonczewski torque) $\tau_{SOT} = m \times (\sigma \times m)$, where σ is the spin accumulation direction[146,147]. The torque leads to the establishment of an effective field $B_{eff} = \sigma \times m$, leading to the magnetization switching. The current-induced magnetization switching for a magnetic TI/non-magnetic TI heterostructure under a small in-plane magnetic field is shown in FIG. 7c (REF.[148]). As current pulses of $\sim 4 \times 10^{10}$ A m^{-2} are applied, the AHE signal changes from positive to negative, which corresponds to a magnetization switching from up to down. The switching current density is approximately one order of magnitude smaller than that needed in ferromagnetic/non-magnetic heterostructures, owing to the large spin Hall angle of TIs. The measurement of the Hall effect using a DC current was reported to lead to an even higher efficiency of current-induced magnetization switching in a magnetic TI/non-magnetic TI heterostructure[121]. However, care should be taken, because the application of a large DC current causes a spurious Hall effect owing to the asymmetric electron–magnon scattering, even without magnetization switching[121,124,148].

For applications, it is desirable that these functionalities are implemented at room temperature. However, at the moment, the Curie temperature of ferromagnetic TIs is a few tens of Kelvins for a moderate doping level and limited to 250 K at the highest doping level[149]. A platform that could overcome this limitation may be a TI/ferromagnetic heterostructure. In fact, nonlinear unidirectional magnetoresistance[150] and current-induced magnetization switching[151–154] have been demonstrated for this type of composite structure or heterostructure. The current-induced magnetization switching in a TI/ferromagnetic heterostructure at room temperature, which is just like the switching in a magnetic TI, is shown in FIG. 7d. The current required for magnetization switching is $\sim 3 \times 10^{10}$ A m^{-2}, showing the potential of TIs as practical spintronic materials[151–154].

Conclusions and perspectives

In the past decade, pioneering theoretical studies have advanced the field of topological quantum science and motivated experimental studies of exotic phenomena in topological materials. In this Review, we have discussed the emergent quantum phenomena in magnetic TIs beyond the experimental confirmation of their topological electronic structures, focusing in particular on their electrical transport and optical properties. Magnetic TIs realize the massive Dirac gap and the materialization of the QAHE and axion insulator state; moreover, they display spintronic functionalities. From a materials science perspective, the key issue regarding the massive Dirac gap with broken time-reversal symmetry is the magnetic doping of the TI to induce the long-range ferromagnetic order. In Cr-doped or V-doped $(Bi,Sb)_2Te_3$, the interaction between surface state electrons and local magnetic moments opens an exchange gap in the Dirac surface state. Heterostructure engineering, including the modulation doping of magnetic ions, raises the temperature at which the QAHE can be observed, providing a concrete platform for the exploration of exotic quantum effects such as the topological magnetoelectric effect and the formation of axion insulators. The functionalization of non-dissipative charge transport will be materialized with the CEMs at magnetic domain walls and, in superconducting heterostructures, chiral Majorana edge modes. Moreover, the interaction between the surface state electrons and the magnetization induces rich spintronic functions, such as current-induced magnetization switching. Here, we discuss the future perspectives for research on magnetic TIs (FIG. 8).

High-temperature realization of the QAHE. The realization of a high-temperature QAHE is necessary for expanding the available experimental techniques to obtain further physical insights into QAH-related phenomena, as well as for the application of dissipationless channels based on the QAHE. Despite the improvements in thin-film growth techniques, such as alloying and heterostructure engineering, the temperature at which the QAHE can be observed is still limited to 2 K (REFS[61,62]). This temperature is far below the Curie temperature

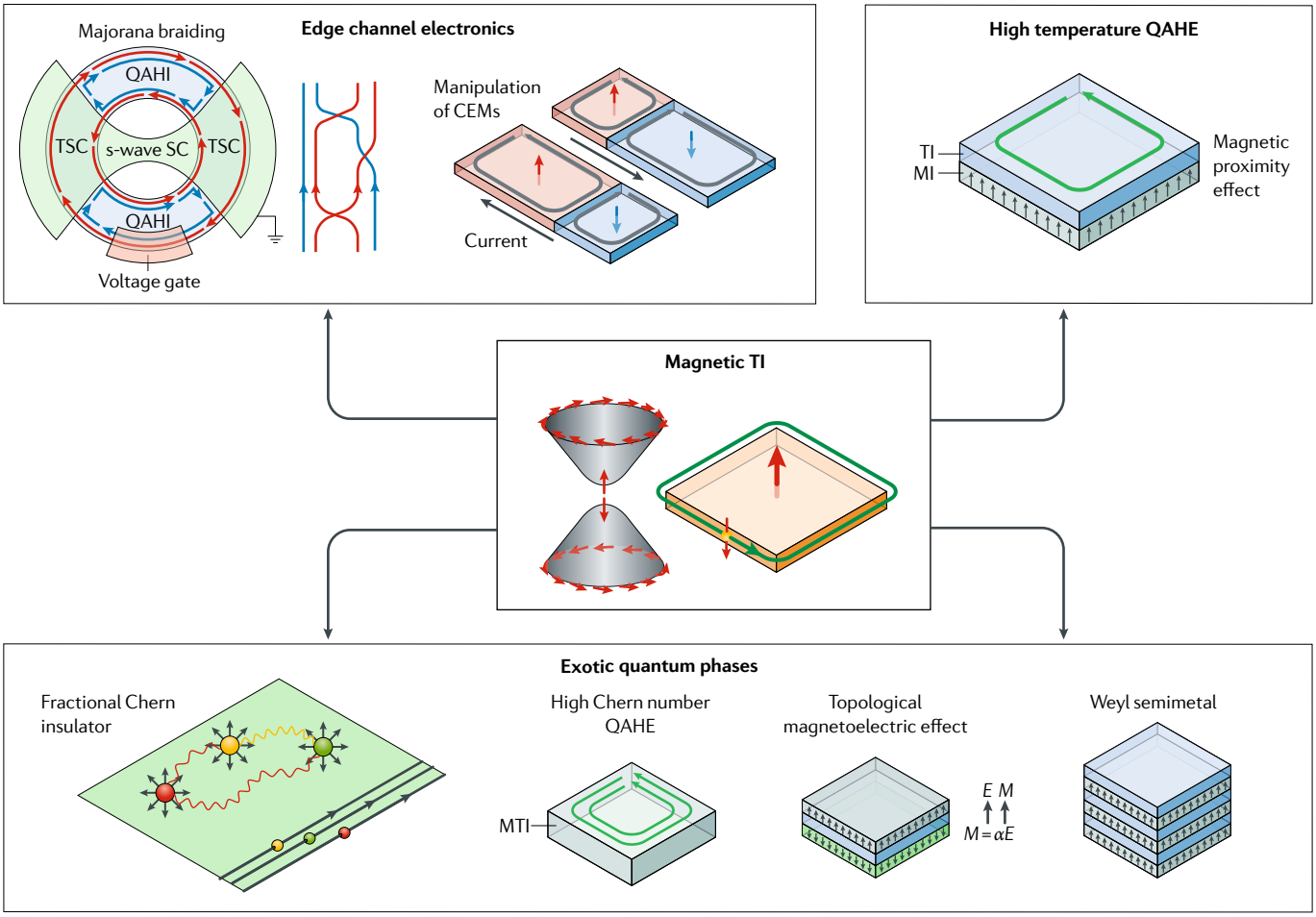

Fig. 8 | **Future perspectives for magnetic topological insulators.** Heterostructure engineering and the development of new measurement techniques will further broaden the field of magnetic topological insulators (TIs). Heterostructures based on magnetic insulators (MIs) and TIs may realize the quantum anomalous Hall effect (QAHE) at high temperatures through magnetic proximity effects. The stacking of MIs and TIs, or of trivial insulators and magnetic TIs, will realize Weyl semimetals through fine tuning of certain parameters, such as the film thickness. The axion term in the Lagrangian of TIs will establish cross relations between magnetism (*M*) and electricity (*E*), yielding quantized topological magnetoelectric effects. A QAHE characterized by high Chern numbers with multiple chiral edge modes (CEMs) will be enabled through appropriate material choices. Nearly flat bands with nontrivial topology will realize a fractional Chern insulator. The proximity to a superconductor, coupled with an elaborate device design, will realize non-Abelian braiding, an important step towards topological quantum computation. Finally, the manipulation of magnetic domain walls by electrical or optical means will enable fast control of CEMs. α, fine structure constant; QAHI, quantum anomalous Hall insulator; SC, superconductor; TSC, topological superconductor. Upper-left panel reproduced with permission from REF.[184], PNAS. Lower-left image reproduced from REF.[93], Springer Nature Limited.

(a few tens of Kelvins) and the magnetization gap energy of the surface state (~500 K). The most plausible reason for the suppression of the observation temperature is disorder in the exchange gap, which is inevitably introduced by the randomly distributed magnetic dopants[50]. An alternative route towards the higher-temperature realization of the QAHE is to leverage the magnetic proximity effect to ferromagnetic insulators with a high Curie temperature[94]. The appropriate selection of the ferromagnetic material and the synthesis of an abrupt interface activating the proximity effect are essential ingredients. The incorporation of the magnetic proximity effect into a TI has been exemplified in heterostructures with magnetic insulators such as EuS (REFS[155–157]), $Cr_2Ge_2Te_6$ (REF.[158]), $Y_3Fe_5O_{12}$ (YIG)[159,160] and $Tm_3Fe_5O_{12}$ (TIG)[161] through measurements that used neutron scattering[157], magnetic second-harmonic generation[156], hysteretic magnetoresistance[159] and the AHE[155,158,160,161]. However, the observed anomalous Hall resistivity was far from the quantized value. This is probably a result of the small magnetization gap resulting from the weak exchange coupling between the magnetic insulator and the TI. A suitable choice of the magnetic insulator yielding strong hybridization with the *p* orbitals of Bi, Sb and Te and the optimization of the heterostructure growth will open new routes towards the high-temperature realization of the QAHE[162].

Another possibility for the realization of a higher-temperature QAHE is to use an intrinsic magnetic TI. One candidate is $MnBi_2Te_4$, which is theoretically

proposed as a layered antiferromagnet with perpendicular magnetic anisotropy[163,164]. The intrinsic magnetization is expected to create a uniform and large magnetization gap and hence to raise the observable temperature of the QAHE. In fact, the gap opening is observed by ARPES[165], and a finite AHE appears in transport measurements[166]. More interestingly, because of its layered antiferromagnetic nature, $MnBi_2Te_4$ is expected to be in a state that changes between the QAH state and an axion insulator state depending on the parity of the number of layers[164].

External control of the QAH state. One of the most attractive features of the QAH state is the topological phase transition, which allows changing the Chern number in a non-volatile way. Thanks to this feature, the magnetization reversal alters the direction of CEMs, the switching between a QAH state and an axion insulator state controls their presence or absence[108–110], and the domain wall motion changes their position[77,79]. To implement CEMs in devices as dissipationless channels, apart from the working-temperature problem, an issue that needs to be solved is the control of the magnetization configuration in a local, rapid and reconfigurable manner. One possibility is to use the spin–orbit torque magnetization switching, exploiting the spin accumulation at the surface state[148]. Another option is to use magneto-optical recording, namely, optical writing of the magnetization through the modulation of the coercivity by heating[167]. The effective control of the magnetic configuration will enable device functionalities based on the domain walls and on magnetoelectric effects, such as reconfigurable dissipationless circuits based on CEMs and reconfigurable microwave circuits based on chiral edge plasmons[168].

Confirmation and control of Majorana modes. Although evidence for chiral Majorana edge modes has been experimentally reported[87], the manipulation of Majorana fermions is still in its infancy. The observation of the quantum coherence of chiral Majorana fermions is the next step towards the realization of topological quantum computation. Some theoretical works propose interferometry between two chiral Majorana edge modes, in which the conductance would be tuned by controlling the phase difference across the junction through the parity of the number of vortices[169,170]. Another proposal is the realization of a Hadamard gate with a Corbino ring junction and a phase gate with the application of a gate voltage[93]. These proposals are experimentally feasible because the quantum states of chiral Majorana edge modes can be read out simply with conductance measurements. From a materials science perspective, the in situ fabrication of heterostructures by molecular beam epitaxy[171] and the strong hybridization of the superconducting state with the TI surface state[172] may realize a large superconducting proximity effect, similar to the magnetic proximity effect.

Materials development towards exotic quantum phases. More exotic quantum states may be implemented with heterostructure engineering and appropriate materials combinations. For example, it was proposed that a magnetic Weyl semimetal would be realized in a superlattice composed of a magnetic TI and a trivial insulator through the tuning of the interlayer and intralayer tunnelling[173,174]. With a single pair of Weyl points in the Brillouin zone, the topologically protected Fermi arc, the nonlocal transport and the chiral anomaly are expected to be observed[175]. The in situ growth of such a heterostructure was realized by using CdSe as a trivial insulator[176]. However, because the trivial insulator was too thick, the superlattice became a simple stacking of QAH states[176]. The fine tuning of the thickness of the trivial insulator will produce a magnetic Weyl semimetal.

QAH states with intrinsically high Chern numbers are proposed to emerge in a magnetic topological crystalline insulator (TCI). TCIs possess four Dirac cones at the surface, protected by band inversion and mirror symmetry. The gapping of the four Dirac cones by magnetization would lead to a QAH insulator with $C = \pm 4$ (REF.[177]). The ferromagnetic order and the AHE are observed in magnetically doped TCIs, such as Cr-doped SnTe thin film, and in magnetic-proximity-coupled SnTe (REFS[178,179]).

The fine tuning of E_F by doping and the improvement of film quality are necessary for the realization of QAH states. Beyond the single band model, the effect of correlations on the topological order will constitute an intriguing issue. The introduction of correlations in magnetic TIs or QAH states will realize fractional quantization without the need for an external magnetic field, in analogy to the fractional QHE under a magnetic field. The choice of suitable materials will be crucial for the realization of nearly flat bands with nontrivial topology[180–184].

All in all, magnetic TIs exhibit rich physics and emergent phenomena and functions. The integration of strong electronic correlations and superconductivity in topological quantum materials will open up new phenomena and research avenues in the near future.

Published online: 18 January 2019

1. Stewart, G. R. Heavy-fermion systems. *Rev. Mod. Phys.* **56**, 755–787 (1984).
2. Lee, P. A., Nagaosa, N. & Wen, X.-G. Doping a Mott insulator: physics of high-temperature superconductivity. *Rev. Mod. Phys.* **78**, 17–85 (2006).
3. Fert, A. Nobel lecture: origin, development, and future of spintronics. *Rev. Mod. Phys.* **80**, 1517–1530 (2008).
4. Tokura, Y. Critical features of colossal magnetoresistive manganites. *Rep. Prog. Phys.* **69**, 797–851 (2006).
5. Dietl, T. & Ohno, H. Dilute ferromagnetic semiconductors: physics and spintronic structures. *Rev. Mod. Phys.* **86**, 187–251 (2014).
6. Hasan, M. Z. & Kane, C. L. Colloquium: topological insulators. *Rev. Mod. Phys.* **82**, 3045–3067 (2010).
7. Qi, X.-L. & Zhang, S.-C. Topological insulators and superconductors. *Rev. Mod. Phys.* **83**, 1057–1110 (2011).
8. Nagaosa, N. & Tokura, Y. Topological properties and dynamics of magnetic skyrmions. *Nat. Nanotechnol.* **8**, 899–911 (2013).
9. Klitzing, Kv, Dorda, G. & Pepper, M. New method for high-accuracy determination of the fine-structure constant based on quantized Hall resistance. *Phys. Rev. Lett.* **45**, 494 (1980).
10. Thouless, D. J., Kohmoto, M., Nightingale, M. P. & den Nijs, M. Quantized Hall conductance in a two-dimensional periodic potential. *Phys. Rev. Lett.* **49**, 405 (1982).
11. Kohmoto, M. Topological invariant and the quantization of the Hall conductance. *Ann. Phys.* **160**, 343 (1985).
12. Haldane, F. D. M. Model for a Quantum hall effect without Landau levels: condensed-matter realization of the "parity anomaly". *Phys. Rev. Lett.* **61**, 2015 (1988).
13. Ohgushi, K., Murakami, S. & Nagaosa, N. Spin anisotropy and quantum Hall effect in the kagomé lattice: chiral spin state based on a ferromagnet. *Phys. Rev. B* **62**, R6065 (2000).
14. Nagaosa, N., Sinova, J., Onoda, S., MacDonald, A. H. & Ong, N. P. Anomalous Hall effect. *Rev. Mod. Phys.* **82**, 1539–1592 (2010).

15. Onoda, M. & Nagaosa, N. Quantized anomalous Hall effect in two-dimensional ferromagnets: quantum Hall effect in metals. *Phys. Rev. Lett.* **90**, 206601 (2003).
16. Chang, C.-Z. et al. Experimental observation of the quantum anomalous Hall effect in a magnetic topological insulator. *Science* **340**, 167–170 (2013).
17. Yu, R. et al. Quantized anomalous Hall effect in magnetic topological insulators. *Science* **329**, 61–64 (2010).
18. Nomura, K. & Nagaosa, N. Surface-quantized anomalous Hall current and the magnetoelectric effect in magnetically disordered topological insulators. *Phys. Rev. Lett.* **106**, 166802 (2011).
19. Kane, C. L. & Mele, E. J. Z_2 topological order and the quantum spin Hall effect. *Phys. Rev. Lett.* **95**, 146802 (2005).
20. Kane, C. L. & Mele, E. J. Quantum spin Hall effect in graphene. *Phys. Rev. Lett.* **95**, 226801 (2005).
21. Fu, L. & Kane, C. L. Topological insulators with inversion symmetry. *Phys. Rev. B* **76**, 045302 (2007).
22. Fu, L., Kane, C. L. & Mele, E. J. Topological insulators in three dimensions. *Phys. Rev. Lett.* **98**, 106803 (2007).
23. Ando, Y. Topological insulator materials. *J. Phys. Soc. Jpn.* **82**, 102001 (2013).
24. Cava, R. J., Ji, H., Fuccillo, M. K., Gibson, Q. D. & Hor, Y. S. Crystal structure and chemistry of topological insulators. *J. Mater. Chem. C.* **1**, 3176–3189 (2013).
25. Zhang, H. et al. Topological insulators in Bi_2Se_3, Bi_2Te_3 and Sb_2Te_3 with a single Dirac cone on the surface. *Nat. Phys.* **5**, 438–442 (2009).
26. Murakami, S. Phase transition between the quantum spin Hall and insulator phases in 3D: emergence of a topological gapless phase. *New J. Phys.* **9**, 356 (2007).
27. Wan, X., Turner, A. M., Vishwanath, A. & Savrasov, S. Y. Topological semimetal and Fermi-arc surface states in the electronic structure of pyrochlore iridates. *Phys. Rev. B* **83**, 205101 (2011).
28. Hasan, M. Z., Xu, S. Y., Belopolski, I. & Huang, S. M. Discovery of Weyl fermion semimetals and topological Fermi arc states. *Annu. Rev. Condens. Matter Phys.* **8**, 289–309 (2017).
29. Fang, Z. et al. The anomalous Hall effect and magnetic monopoles in momentum space. *Science* **302**, 92–95 (2003).
30. Heremans, J. P., Cava, R. J. & Samarth, N. Tetradymites as thermoelectrics and topological insulators. *Nat. Rev. Mater.* **2**, 17049 (2017).
31. Kou, X., Fan, Y., Lang, M., Upadhyaya, P. & Wang, K. L. Magnetic topological insulators and quantum anomalous hall effect. *Sol. St. Commun.* **215**, 34–53 (2015).
32. Chang, C.-Z. & Li, M. Quantum anomalous Hall effect in time-reversal-symmetry breaking topological insulators. *J. Phys. Condens. Matter* **28**, 123002 (2016).
33. Ke, H., Wang, Y. & Xue, Q.-K. Topological materials: quantum anomalous Hall system. *Annu. Rev. Cond. Mat. Phys.* **9**, 329–344 (2018).
34. Biswas, R. R. & Balatsky, A. V. Impurity-induced states on the surface of three-dimensional topological insulators. *Phys. Rev. B* **81**, 233405 (2010).
35. Rosenberg, G. & Franz, M. Surface magnetic ordering in topological insulators with bulk magnetic dopants. *Phys. Rev. B* **85**, 195119 (2012).
36. Henk, J. et al. Complex spin texture in the pure and Mn-doped topological insulator Bi_2Te_3. *Phys. Rev. Lett.* **108**, 206801 (2012).
37. Zhang, J.-M., Zhu, W., Zhang, Y., Xiao, D. & Yao, Y. Tailoring magnetic doping in the topological insulator Bi_2Se_3. *Phys. Rev. Lett.* **109**, 266405 (2012).
38. Kacman, P. Spin interactions in diluted magnetic semiconductors and magnetic semiconductors. *Semicond. Sci. Technol.* **16**, R25–R39 (2001).
39. Dietl, T., Ohno, H. & Matsukura, F. Hole-mediated ferromagnetism in tetrahedrally coordinated semiconductors. *Phys. Rev. B* **63**, 195205 (2001).
40. Dietl, T. & Ohno, H. Ferromagnetic III-V and II-VI semiconductors. *MRS Bull.* **28**, 714–719 (2003).
41. Liu, Q., Liu, C.-X., Xu, C., Qi, X.-L. & Zhang, S.-C. Magnetic impurities on the surface of a topological insulator. *Phys. Rev. Lett.* **102**, 156603 (2009).
42. Abanin, D. A. & Pesin, D. A. Ordering of magnetic impurities and tunable electronic properties of topological insulators. *Phys. Rev. Lett.* **106**, 136802 (2011).
43. Zhu, J.-J., Yao, D.-X., Zhang, S.-C. & Chang, K. Electrically controllable surface magnetism on the surface of topological insulators. *Phys. Rev. Lett.* **106**, 097201 (2011).
44. Hor, Y. S. et al. Development of ferromagnetism in the doped topological insulator $Bi_{2-x}Mn_xTe_3$. *Phys. Rev. B* **81**, 195203 (2010).
45. Checkelsky, J. G. et al. Dirac-fermion-mediated ferromagnetism in a topological insulator. *Nat. Phys.* **8**, 729–733 (2012).
46. Sessi, P. et al. Signature of Dirac fermion-mediated magnetic order. *Nat. Commun.* **5**, 5349 (2014).
47. Chang, C.-Z. et al. Thin films of magnetically doped topological insulator with carrier-independent long-range ferromagnetic order. *Adv. Mater.* **25**, 1065–1070 (2013).
48. Li, M. et al. Experimental verification of the Van Vleck nature of long-range ferromagnetic order in the vanadium-doped three-dimensional topological insulator Sb_2Te_3. *Phys. Rev. Lett.* **114**, 146802 (2015).
49. Kou, X. et al. Interplay between different magnetisms in Cr-doped topological insulators. *ACSNano* **7**, 9205–9212 (2013).
50. Lee, I. et al. Imaging Dirac-mass disorder from magnetic dopant atoms in the ferromagnetic topological insulator $Cr_x(Bi_{0.1}Sb_{0.9})_{2-x}Te_3$. *Proc. Natl Acad. Sci. USA* **112**, 1316–1321 (2015).
51. Chen, Y. L. et al. Massive Dirac fermion on the surface of a magnetically doped topological insulator. *Science* **329**, 659–662 (2010).
52. Wray, L. A. et al. A topological insulator surface under strong Coulomb, magnetic and disorder perturbations. *Nat. Phys.* **7**, 32–37 (2011).
53. Xu, S.-Y. et al. Hedgehog spin texture and Berry's phase tuning in a magnetic topological insulator. *Nat. Phys.* **8**, 616–622 (2012).
54. Sessi, P. et al. Dual nature of magnetic dopants and competing trends in topological insulators. *Nat. Commun.* **7**, 12027 (2016).
55. Krieger, J. A. et al. Spectroscopic perspective on the interplay between electronic and magnetic properties of magnetically doped topological insulators. *Phys. Rev. B* **96**, 184402 (2017).
56. Chang, C.-Z. et al. High-precision realization of robust quantum anomalous Hall state in a hard ferromagnetic topological insulator. *Nat. Mater.* **14**, 473–477 (2015).
57. Wang, J., Lian, B., Zhang, H. & Zhang, S. C. Anomalous edge transport in the quantum anomalous Hall state. *Phys. Rev. Lett.* **111**, 086803 (2013).
58. Kou, X. et al. Scale-invariant quantum anomalous Hall effect in magnetic topological insulators beyond the two-dimensional limit. *Phys. Rev. Lett.* **113**, 137201 (2014).
59. Bestwick, A. J. et al. Precise quantization of the anomalous Hall effect near zero magnetic field. *Phys. Rev. Lett.* **114**, 187201 (2015).
60. Chang, C.-Z. et al. Zero-field dissipationless chiral edge transport and the nature of dissipation in the quantum anomalous Hall state. *Phys. Rev. Lett.* **115**, 057206 (2015).
61. Mogi, M. et al. Magnetic modulation doping in topological insulators toward higher-temperature quantum anomalous Hall effect. *Appl. Phys. Lett.* **107**, 182401 (2015).
62. Ou, Y. et al. Enhancing the quantum anomalous Hall effect by magnetic codoping in a topological insulator. *Adv. Mater.* **30**, 1703062 (2018).
63. Checkelsky, J. G. et al. Trajectory of the anomalous Hall effect towards the quantized state in a ferromagnetic topological insulator. *Nat. Phys.* **10**, 731–736 (2014).
64. Kou, X. et al. Metal-to-insulator switching in quantum anomalous Hall states. *Nat. Commun.* **6**, 8474 (2015).
65. Chang, C.-Z. et al. Observation of the quantum anomalous Hall insulator to Anderson insulator quantum phase transition and its scaling behavior. *Phys. Rev. Lett.* **117**, 126802 (2016).
66. Kawamura, M. et al. Current-driven instability of the quantum anomalous Hall effect in ferromagnetic topological insulators. *Phys. Rev. Lett.* **119**, 016803 (2017).
67. Fox, E. J. et al. Part-per-million quantization and current-induced breakdown of the quantum anomalous Hall effect. *Phys. Rev. B* **98**, 075145 (2018).
68. Kawamura, M. et al. Topological quantum phase transition in magnetic topological insulator upon magnetization rotation. *Phys. Rev. B* **98**, 140404 (2018).
69. Liu, C.-X., Qi, X.-L., Dai, X., Fang, Z. & Zhang, S.-C. Quantum anomalous Hall effect in $Hg_{1-y}Mn_yTe$ quantum wells. *Phys. Rev. Lett.* **101**, 146802 (2008).
70. Jeckelmann, B. & Jeanneret, B. The quantum Hall effect as an electrical resistance standard. *Rep. Prog. Phys.* **64**, 1603–1655 (2001).
71. Scherer, H. & Camarota, B. Quantum metrology triangle experiments: a status review. *Meas. Sci. Technol.* **23**, 124010 (2012).
72. Gotz, M. et al. Precision measurement of the quantized anomalous Hall resistance at zero magnetic field. *Appl. Phys. Lett.* **112**, 072102 (2018).
73. Kaneko, N. Review of quantum electrical standards and benefits and effects of the implementation of the 'Revised SI'. *IEEJ Trans.* **12**, 627–637 (2017).
74. Ribeiro-Palau, R. et al. Quantum Hall resistance standard in graphene devices under relaxed experimental conditions. *Nat. Nanotechnol.* **10**, 965–972 (2015).
75. Upadhyaya, P. & Tserkovnyak, Y. Domain wall in a quantum anomalous Hall insulator as a magnetoelectric piston. *Phys. Rev. B* **94**, 020411 (2016).
76. Liu, M. et al. Large discrete jumps observed in the transition between Chern states in a ferromagnetic topological insulator. *Sci. Adv.* **2**, e1600167 (2016).
77. Yasuda, K. et al. Quantized chiral edge conduction on domain walls of a magnetic topological insulator. *Science* **358**, 1311–1314 (2017).
78. Büttiker, M. Absence of backscattering in the quantum Hall effect in multiprobe conductors. *Phys. Rev. B* **38**, 9375–9389 (1988).
79. Rosen, I. T. et al. Chiral transport along magnetic domain walls in the quantum anomalous Hall effect. *NPJ Quantum Mater.* **2**, 69 (2017).
80. Fu, L. & Kane, C. L. Superconducting proximity effect and majorana fermions at the surface of a topological insulator. *Phys. Rev. Lett.* **100**, 096407 (2008).
81. Qi, X.-L., Hughes, T. L. & Zhang, S.-C. Chiral topological superconductor from the quantum Hall state. *Phys. Rev. B* **82**, 184516 (2010).
82. Wang, J., Zhou, Q., Lian, B. & Zhang, S.-C. Chiral topological superconductor and half-integer conductance plateau from quantum anomalous Hall plateau transition. *Phys. Rev. B* **92**, 064520 (2015).
83. Majorana, E. Teoria simmetrica dell'elettrone e del positrone. *Nuovo Cim.* **14**, 171–184 (1937).
84. Kitaev, A. Y. Anyons in an exactly solved model and beyond. *Ann. Phys.* **321**, 2–111 (2006).
85. Wilczek, F. Majorana returns. *Nat. Phys.* **5**, 614–618 (2009).
86. Alicea, J. New directions in the pursuit of Majorana fermions in solid state systems. *Rep. Prog. Phys.* **75**, 076501 (2012).
87. He, Q. L. et al. Chiral Majorana fermion modes in a quantum anomalous Hall insulator–superconductor structure. *Science* **357**, 294–299 (2017).
88. Wang, J., Lian, B. & Zhang, S.-C. Universal scaling of the quantum anomalous Hall plateau transition. *Phys. Rev. B* **89**, 085106 (2014).
89. Feng, Y. et al. Observation of the zero Hall plateau in a quantum anomalous Hall insulator. *Phys. Rev. Lett.* **115**, 126801 (2015).
90. Huang, Y., Setiawan, F. & Sau, J. D. Disorder-induced half-integer quantized conductance plateau in quantum anomalous Hall insulator-superconductor structures. *Phys. Rev. B* **97**, 100501(R) (2018).
91. Ji, W. & Wen, X.-G. $1/2(e^2/h)$ conductance plateau without 1D chiral Majorana fermions. *Phys. Rev. Lett.* **120**, 107002 (2018).
92. Lian, B., Wang, J., Sun, X.-Q., Vaezi, A. & Zhang, S.-C. Quantum phase transition of chiral Majorana fermions in the presence of disorder. *Phys. Rev. B* **97**, 125408 (2018).
93. Lian, B., Sun, X.-Q., Vaezi, A., Qi, X.-L. & Zhang, S.-C. Topological quantum computation based on chiral Majorana fermions. *Proc. Natl Acad. Sci. USA* **115**, 10938–10942 (2018).
94. Qi, X. L., Hughes, T. L. & Zhang, S. C. Topological field theory of time-reversal invariant insulators. *Phys. Rev. B* **78**, 195424 (2008).
95. Peccei, R. D. & Quinn, H. R. CP conservation in the presence of pseudoparticles. *Phys. Rev. Lett.* **38**, 1440 (1977).
96. Essin, A. M., Moore, J. E. & Vanderbilt, D. Magnetoelectric polarizability and axion electrodynamics in crystalline insulators. *Phys. Rev. Lett.* **102**, 146805 (2009).
97. Tokura, Y., Seki, S. & Nagaosa, N. Mulrtiferroics of spin origin. *Rep. Prog. Phys.* **77**, 076501 (2014).
98. Freeman, A. J. & Schmid, H. *Magnetoelectric interaction phenomena in crystals* (Gordon and Breach Science Publishers London, 1975).
99. Kurumaji, T. et al. Optical magnetoelectric resonance in a polar magnet $(Fe,Zn)_2Mo_3O_8$ with

axion-type coupling. *Phys. Rev. Lett.* **119**, 077206 (2017).
100. Tse, W.-K. & MacDonald, A. H. Giant magneto-optical Kerr effect and universal Faraday effect in thin-film topological insulators. *Phys. Rev. Lett.* **105**, 057401 (2010).
101. Maciejko, J., Qi, X.-L., Drew, H. D. & Zhang, S.-C. Topological quantization in units of the fine structure constant. *Phys. Rev. Lett.* **105**, 166803 (2010).
102. Okada, K. N. et al. Terahertz spectroscopy on Faraday and Kerr rotations in a quantum anomalous Hall state. *Nat. Commun.* **7**, 12245 (2016).
103. Liang., W. et al. Quantized Faraday and Kerr rotation and axion electrodynamics of a 3D topological insulator. *Science* **354**, 1124–1127 (2016).
104. Dziom, V. et al. Observation of the universal magnetoelectric effect in a 3D topological insulator. *Nat. Commun.* **8**, 15197 (2017).
105. Armitage, N. P. & Wu, L. On the matter of topological insulators as magnetoelectrics. Preprint at https://arxiv.org/abs/1810.01233 (2018).
106. Morimoto, T., Furusaki, A. & Nagaosa, N. Topological magnetoelectric effects in thin films of topological insulators. *Phys. Rev. B* **92**, 085113 (2015).
107. Wang, J., Lian, B., Qi, X.-L. & Zhang, S.-C. Quantized topological magnetoelectric effect of the zero-plateau quantum anomalous Hall state. *Phys. Rev. B* **92**, 081107(R) (2015).
108. Mogi, M. et al. A magnetic heterostructure of topological insulators as a candidate for an axion insulator. *Nat. Mater.* **16**, 516–521 (2017).
109. Mogi, M. et al. Tailoring tricolor structure of magnetic topological insulator for robust axion insulator. *Sci. Adv.* **3**, eaao1669 (2017).
110. Xiao, D. et al. Realization of the axion insulator state in quantum anomalous Hall sandwich heterostructures. *Phys. Rev. Lett.* **120**, 056801 (2018).
111. Edelstein, V. M. Spin polarization of conduction electrons induced by electric current in two-dimensional asymmetric electron systems. *Solid State Commun.* **73**, 233 (1990).
112. Kondou, K. et al. Fermi-level-dependent charge-to-spin current conversion by Dirac surface states of topological insulators. *Nat. Phys.* **12**, 1027–1031 (2016).
113. Mellnik, A. R. et al. Spin–transfer torque generated by a topological insulator. *Nature* **511**, 449–451 (2014).
114. Wang, Y. et al. Topological surface states originated spin–orbit torques in Bi_2Se_3. *Phys. Rev. Lett.* **114**, 257202 (2015).
115. Shiomi, Y. et al. Spin-electricity conversion induced by spin injection into topological insulators. *Phys. Rev. Lett.* **113**, 196601 (2014).
116. Deorani, P. et al. Observation of inverse spin Hall effect in bismuth selenide. *Phys. Rev. B* **90**, 094403 (2014).
117. Jamali, M. et al. Giant spin pumping and inverse spin Hall effect in the presence of surface and bulk spin–orbit coupling of topological insulator Bi_2Se_3. *Nano Lett.* **15**, 7126–7132 (2015).
118. Mendes, J. B. S. et al. Dirac-surface-state-dominated spin to charge current conversion in the topological insulator $(Bi_{0.22}Sb_{0.78})_2Te_3$ films at room temperature. *Phys. Rev. B* **96**, 180415 (2017).
119. Wang, H. et al. Surface-state-dominated spin–charge current conversion in topological-insulator/ferromagnetic-insulator heterostructures. *Phys. Rev. Lett.* **117**, 076601 (2016).
120. Liu, L. et al. Spin-polarized tunneling study of spin-momentum locking in topological insulators. *Phys. Rev. B* **91**, 235437 (2015).
121. Fan, Y. et al. Magnetization switching through giant spin–orbit torque in a magnetically doped topological insulator heterostructure. *Nat. Mater.* **13**, 699–704 (2014).
122. Yasuda, K. et al. Geometric Hall effects in topological insulator heterostructures. *Nat. Phys.* **12**, 555–559 (2016).
123. Han, W., Otani, Y. & Maekawa, S. Quantum materials for spin and charge conversion. *NPJ Quantum Mater.* **3**, 27 (2018).
124. Yabin, F. et al. Electric-field control of spin–orbit torque in a magnetically doped topological insulator. *Nat. Nanotechol.* **11**, 352–359 (2016).
125. Jiang., Z. et al. Enhanced spin Seebeck effect signal due to spin-momentum locked topological surface states. *Nat. Commun.* **7**, 11458 (2016).
126. Olejník, K., Novák, V., Wunderlich, J. & Jungwirth, T. Electrical detection of magnetization reversal without auxiliary magnets. *Phys. Rev. B* **91**, 180402 (2015).
127. Avci, C. O. et al. Unidirectional spin Hall magnetoresistance in ferromagnet/normal metal bilayers. *Nat. Phys.* **11**, 570–575 (2015).
128. Avci, C. O. et al. Magnetoresistance of heavy and light metal/ferromagnet bilayers. *Appl. Phys. Lett.* **107**, 192405 (2015).
129. Yasuda, K. et al. Large unidirectional magnetoresistance in a magnetic topological insulator. *Phys. Rev. Lett.* **117**, 127202 (2016).
130. Tokura, Y. & Nagaosa, N. Nonreciprocal responses from non-centrosymmetric quantum materials. *Nat. Commun.* **9**, 3740 (2018).
131. Baibich, M. N. et al. Giant magnetoresistance of (001) Fe/(001) Cr magnetic superlattices. *Phys. Rev. Lett.* **61**, 2472 (1988).
132. Binasch, G., Grünberg, P., Saurenbach, F. & ZinnEnhanced, W. magnetoresistance in layered magnetic structures with antiferromagnetic interlayer exchange. *Phys. Rev. B* **39**, 4828 (1989).
133. Yoshimi, R. et al. Quantum Hall states stabilized in semi-magnetic bilayers of topological insulators. *Nat. Commun.* **6**, 8530 (2015).
134. Ogawa, N. et al. Zero-bias photocurrent in ferromagnetic topological insulator. *Nat. Commun.* **7**, 12246 (2016).
135. Grinberg, I. et al. Perovskite oxides for visible-light-absorbing ferroelectric and photovoltaic materials. *Nature* **503**, 509–512 (2013).
136. Ogawa, N., Sotome, M., Kaneko, Y., Ogino, M. & Tokura, Y. Shift current in the ferroelectric semiconductor SbSI. *Phys. Rev. B* **96**, 241203 (2017).
137. McIver, J. W., Hsieh, D., Steinberg, H., Jarillo-Herrero, P. & Gedik, N. Control over topological insulator photocurrents with light polarization. *Nat. Nanotech.* **7**, 96–100 (2012).
138. Okada, K. N. et al. Enhanced photogalvanic current in topological insulators via Fermi energy tuning. *Phys. Rev. B* **93**, 081403 (2016).
139. Fert, A., Reyren, N. & Cros, V. Magnetic skyrmions: advances in physics and potential applications. *Nat. Rev. Mater.* **2**, 17031 (2017).
140. Liu, C. et al. Dimensional crossover-induced topological Hall effect in a magnetic topological insulator. *Phys. Rev. Lett.* **119**, 176809 (2017).
141. He, Q. L. et al. Exchange-biasing topological charges by antiferromagnetism. *Nat. Commun.* **9**, 2767 (2018).
142. Miron, I. M. et al. Perpendicular switching of a single ferromagnetic layer induced by in-plane current injection. *Nature* **476**, 189–193 (2011).
143. Liu, L., Lee, O. J., Gudmundsen, T. J., Ralph, D. C. & Buhrman, R. A. Current-induced switching of perpendicularly magnetized magnetic layers using spin torque from the spin Hall effect. *Phys. Rev. Lett.* **109**, 096602 (2012).
144. Liu, L. et al. Spin-torque switching with the giant spin Hall effect of tantalum. *Science* **336**, 555–558 (2012).
145. Pai, C. F. et al. Spin transfer torque devices utilizing the giant spin Hall effect of tungsten. *Appl. Phys. Lett.* **101**, 122404 (2012).
146. Slonczewski, J. C. Current-driven excitation of magnetic multilayers. *J. Magn. Magn. Mat.* **159**, L1–L7 (1996).
147. Ralph, D. C. & Stiles, M. D. Spin transfer torques. *J. Magn. Magn. Mat.* **230**, 1190–1216 (2008).
148. Yasuda, K. et al. Current-nonlinear Hall effect and spin-orbit torque magnetization switching in a magnetic topological insulator. *Phys. Rev. Lett.* **119**, 137204 (2017).
149. Gupta, S., Kanai, S., Matsukura, F. & Ohno, H. Magnetic and transport properties of Sb_2Te_3 doped with high concentration of Cr. *Appl. Phys. Express* **10**, 103001 (2017).
150. Lv, Y. et al. Unidirectional spin-Hall and Rashba–Edelstein magnetoresistance in topological insulator-ferromagnet layer heterostructures. *Nat. Commun.* **9**, 111 (2018).
151. Han, J. et al. Room-temperature spin–orbit torque switching induced by a topological insulator. *Phys. Rev. Lett.* **119**, 077702 (2017).
152. Wang, Y. et al. Room temperature magnetization switching in topological insulator–ferromagnet heterostructures by spin–orbit torques. *Nat. Commun.* **8**, 1364 (2017).
153. Khang, N. H. D., Ueda, Y. & Hai, P. N. A conductive topological insulator with colossal spin Hall effect for ultra-low power spin-orbit-torque switching. *Nat. Mater.* **17**, 808–813 (2018).
154. DC, M. et al. Room-temperature perpendicular magnetization switching through giant spin-orbit torque from sputtered $Bi_xSe_{(1-x)}$ topological insulator material. *Nat. Mater.* **17**, 800–807 (2018).
155. Wei, P. et al. Exchange-coupling-induced symmetry breaking in topological insulators. *Phys. Rev. Lett.* **110**, 186807 (2013).
156. Lee, C., Katmis, F., Jarillo-Herrero, P., Moodera, J. S. & Gedik, N. Direct measurement of proximity-induced magnetism at the interface between a topological insulator and a ferromagnet. *Nat. Commun.* **7**, 12014 (2016).
157. Katmis, F. et al. A high-temperature ferromagnetic topological insulating phase by proximity coupling. *Nature* **533**, 513–516 (2016).
158. Alegria, L. D. et al. Large anomalous Hall effect in ferromagnetic insulator-topological insulator heterostructures. *Appl. Phys. Lett.* **105**, 053512 (2014).
159. Lang, M. et al. Proximity induced high-temperature magnetic order in topological insulator-ferrimagnetic insulator heterostructure. *Nano Lett.* **14**, 3459–3465 (2014).
160. Jiang, Z. et al. Independent tuning of electronic properties and induced ferromagnetism in topological insulators with heterostructure approach. *Nano Lett.* **15**, 5835–5840 (2015).
161. Tang, C. et al. Above 400-K robust perpendicular ferromagnetic phase in a topological insulator. *Sci. Adv.* **3**, e1700307 (2017).
162. Otrokov, M. M. et al. Highly-ordered wide bandgap materials for quantized anomalous Hall and magnetoelectric effects. *2D Mater.* **4**, 025082 (2017).
163. Zhang, D., Shi, M., Xing, D., Zhang, H. & Wang, J. Topological axion states in magnetic insulator $MnBi_2Te_4$ with the quantized magnetoelectric effect. Preprint at https://arxiv.org/abs/1808.08014 (2018).
164. Li, J. et al. Intrinsic magnetic topological insulators in van der Waals layered $MnBi_2Te_4$-family materials. Preprint at https://arxiv.org/abs/1808.08608 (2018).
165. Otrokov, M. M. et al. Prediction and observation of the first antiferromagnetic topological insulator. Preprint at https://arxiv.org/abs/1809.07389 (2018).
166. Gong, Y. et al. Experimental realization of an intrinsic magnetic topological insulator. Preprint at https://arxiv.org/abs/1809.07926 (2018).
167. Yeats, A. L. et al. Local optical control of ferromagnetism and chemical potential in a topological insulator. *Proc. Natl Acad. Sci. USA* **114**, 10379–10383 (2017).
168. Mahoney, A. C. et al. Zero-field edge plasmons in a magnetic topological insulator. *Nat. Commun.* **8**, 1836 (2017).
169. Fu, L. & Kane, C. L. Probing neutral Majorana fermion edge modes with charge transport. *Phys. Rev. Lett.* **102**, 216403 (2009).
170. Akhmerov, A. R., Nilsson, J. & Beenakker, C. W. J. Electrically detected interferometry of Majorana fermions in a topological insulator. *Phys. Rev. Lett.* **102**, 216404 (2009).
171. Schuffelgen, P. et al. Stencil lithography of superconducting contacts on MBE-grown topological insulator thin films. *J. Cryst. Growth* **477**, 183–187 (2017).
172. He, Q. L. et al. Two-dimensional superconductivity at the interface of a Bi_2Te_3/FeTe heterostructure. *Nat. Commun.* **5**, 4247 (2014).
173. Burkov, A. A. & Balents, L. Weyl semimetal in a topological insulator multilayer. *Phys. Rev. Lett.* **107**, 127205 (2011).
174. Balents, L. Viewpoint: Weyl electrons kiss. *Physics* **4**, 36 (2011).
175. Armitage, N. P., Mele, E. J. & Vishwanath, A. Weyl and Dirac semimetals in three-dimensional solids. *Rev. Mod. Phys.* **90**, 015001 (2018).
176. Jiang, G. et al. Quantum anomalous Hall multilayers grown by molecular beam epitaxy. *Chin. Phys. Lett.* **35**, 076802 (2018).
177. Fang, C., Gilbert, M. J. & Bernevig, B. A. Large-Chern-number quantum anomalous Hall effect in thin-film topological crystalline insulators. *Phys. Rev. Lett.* **112**, 046801 (2014).
178. Assaf, B. A. et al. Inducing magnetism onto the surface of a topological crystalline insulator. *Phys. Rev. B* **91**, 195310 (2015).
179. Wang, F. et al. Chromium-induced ferromagnetism with perpendicular anisotropy in topological crystalline insulator SnTe (111) thin films. *Phys. Rev. B* **97**, 115414 (2018).
180. Tang, E., Mei, J. W. & Wen, X. G. High-temperature fractional quantum Hall states. *Phys. Rev. Lett.* **106**, 236802 (2011).
181. Sun, K., Gu, Z., Katsura, H. & Sarma, S. D. Nearly flatbands with nontrivial topology. *Phys. Rev. Lett.* **106**, 236803 (2011).

182. Neupert, T., Santos, L., Chamon, C. & Mudry, C. Fractional quantum Hall states at zero magnetic field. *Phys. Rev. Lett.* **106**, 236804 (2011).
183. Klinovaja, J., Tserkovnyak, Y. & Loss, D. Integer and fractional quantum anomalous Hall effect in a strip of stripes model. *Phys. Rev. B* **91**, 085426 (2015).
184. Maciejko, J. & Fiete, G. A. Fractionalized topological insulators. *Nat. Phys.* **11**, 385–388 (2015).

Acknowledgements
The authors thank R. Yoshimi, M. Mogi, M. Kawamura, N. Nagaosa, M. Kawasaki and T. Dietl for enlightening discussions on magnetic topological insulators. This research was supported in part by the Japan Society for the Promotion of Science (JSPS; no. 16J03476), the Ministry of Education, Culture, Sports, Science and Technology (MEXT), Japan (no. JP15H05853), and Core Research for Evolutional Science and Technology (CREST), Japanese Science and Technology (JST; no. JPMJCR16F1).

Author contributions
All authors have read, discussed and contributed to the writing of the manuscript.

Competing interests statement
The authors declare no competing interests.

Publisher's note
Springer Nature remains neutral with regard to jurisdictional claims in published maps and institutional affiliations.